Influence of Venturi Tube Geometry and Particle Properties on the Hydrodynamic Cavitation for Fine Particle Flotation

by

Mingda Li

A thesis submitted in partial fulfillment of the requirements for the degree of

Master of Science

in

Chemical Engineering

Department of Chemical and Materials Engineering

University of Alberta

ABSTRACT

In this study, the influences of both Venturi tube geometry and particle properties on the hydrodynamic cavitation are investigated. In the geometry study, we investigated numerically and experimentally the influence of several geometrical parameters on the cavitation inception and bubble generation. Using a dimensionless number analysis, an inverse relation is found between the cavitation inception and the single-phase flow resistance set by the geometry. In the cavitation regime, the flow resistance induced by cavitation follows a single trend regardless of the studied geometries. The small outlet angle associated with low inception velocity was found to be favorable for cavitation activities. Moreover, the amount of bubbles generated was found to be correlated to extra flow resistance induced by the cavitation process and the dissolved gas concentration. The insights gained in this study provided a guideline to design efficient Venturi tube in regard to the cavitation process for fine particle flotation. In industrial applications in mineral processing, fluid under hydrodynamic cavitation has large amount of particle content with different properties. In this work, the changes in cavitation behavior were examined with the particles of different surface properties. The results were quantified by dimensionless number method developed in the geometry study. In comparison with water, the hydrophobic particles were found to be favorable for cavitation. Finally, the significant drop in cavitation inception velocity with bubble injection was observed by using the existing equipment and experimental methods.

ACKNOWLEDGEMENT

I would like to express my sincere gratitude to my supervisor, Prof. Qingxia (Chad) Liu for his support and enthusiastic encouragement during my graduate studies. The knowledge and skills I have gained over this time will undoubtedly serve me well as I move forward on to the next stage of my life.

I would like to express great appreciation to my advisor, Dr. Adrien Bussonnière who has pushed me to look at things under a different perspective. His support has been invaluable.

I would like to thank Mr. Carl Corbett for his knowledge and assistance in the equipment design and setup that was used for this project.

I would also like to thank the co-op and summer students Matt Bronson, Brian Leung, Angela Xue, Owais Khalid and Vitalii Dodonov for their help re-running these tests to gather the data.

I would like to thank Prof. Zhenghe Xu for allowing me to borrow and use different lab equipment. Without his generous contribution, I would not have been able to finish this thesis.

I would like to express my appreciation to all the colleagues from the research group for all their support and assistance.

I would like to acknowledge the financial support from Natural Science and Engineering Research Council of Canada (NSERC), the Canadian Centre for Clean Coal/Carbon and Mineral Processing Technologies (C^5MPT) and Canadian Mining Industry Resource Organization (CAMIRO).

Table of Contents

List of Figures

List of Tables

NOMENCLATURE

A	Reference area
c_d	Drag coefficient
c_w	Concentration of solids by weight
d	Venturi tube throat diameter
D	Venturi tube inlet and outlet diameter
D_b	Bubble diameter
D_p	Particle diameter
E_b	Energy barrier for a bubble to form
F_d	Drag force
f	Cumulative distribution fraction
L	Venturi tube throat length
L_c	Loss coefficient
L_{c0}	Mean system loss
P	Power consumption
P^{in}	Power consumption at inception
P_t	Total collection probability
P_a	Attachment probability
P_c	Collision probability
P_d	Detachment probability
p_d	Pressure at downstream of the Venturi tube
p_g	Gas partial pressure
p_u	Pressure at upstream of the Venturi tube

p_v	Vapor pressure
Q	Flow rate
r_b	Bubble radius
s	Standard deviation
u_b	Bubble rising velocity
v	Flow velocity
v_{th}	Flow velocity at the Venturi tube throat
Re	Reynolds number
ΔP	Pressure difference between vapor and liquid pressure
α	Venturi tube convergent or inlet angle
β	Venturi tube divergent or outlet angle
γ_c	Critical wetting surface tension
γ_{LV}	Liquid-gas surface tension
μ	Mean of the cumulative distribution
μ_l	Liquid density
θ	Contact angle
ρ	Mass density of the mixture
ρ_s	Mass density of the solid
ρ_l	Mass density of the liquid
σ	Cavitation number
σ_d	Downstream cavitation number
σ_d^{in}	Downstream cavitation number at inception
σ_u	Upstream cavitation number

ABBREVIATIONS

BS	Bare Silica
BSE	Back-scattered electrons
CFD	Computational fluid dynamics
DMDCS	Dimethyldichlorosilane
GB	Glass bead
HC	Hydrodynamic cavitation
LBM	Lattice Boltzmann Method
SE	Secondary electrons
SEM	Scanning electron microscope
SLA	Stereolithography
TS	Treated silica

Chapter 1 Introduction

1.1 Background

Froth flotation is a commonly used mineral extraction process utilizing the air bubbles to attach onto target minerals for separation from other solid particles with different surface wettabilities (Yoon and Luttrell 1986, 1997). In the flotation process, rising bubbles injected from the column bottom collide with, and attach to the hydrophobic particles. If the bubble-particle agglomerate has an overall density less than the liquid phase, the targeted mineral is brought to the top froth layer, leaving the rest of particles discharged from the column bottom. In the flotation process, the probability of particle collection, P_t, is determined by three micro-scale processes factors (Figure 1-1) (Yoon and Luttrell, 1986; Tao 2005) defined as:

$$P_t = P_c P_a (1 - P_d) \tag{1.1}$$

where P_c is the bubble/particle collision probability, P_a is the bubble/particle attachment probability, and P_d is the bubble/particle detachment probability. The collision probability P_c can be quantified as the fraction of particles that collide with a rising bubble (Weber and Paddock, 1983; Yoon and Luttrell, 1986) defined as:

$$P_c = \frac{3}{2}\left(\frac{D_p}{D_b}\right)^2\left[1 + \frac{\frac{3}{16}R_{eb}}{1+0.249{R_e}^{0.56}}\right] \tag{1.2}$$

where D_p and D_b are the particle and bubble diameter respectively. *Reb* is the bubble Reynolds number defined as:

$$Re = \frac{\rho_l u_b D_b}{\mu_l} \tag{1.3}$$

where p_l is the liquid density, u_b is the terminal bubble rising velocity, and μ_l stands for the liquid viscosity. Equation (1.2) is valid for rigid spheres of D_p/D_b<0.1 in the range of 0< Re<300. As shown in the equation, P_c is proportional to the square of particle diameter, while inversely proportional to the square of the bubble diameter. With a good consistency to the theory, it is experimentally proved that P_c drops rapidly with increasing D_b (Yoon and Luttrell, 1986; Parkinson and Ralston, 2011).

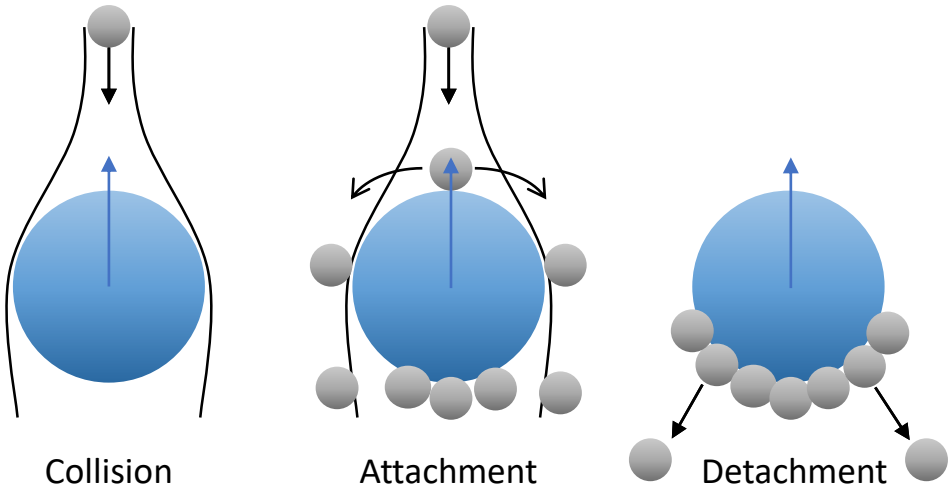

Figure 1-1. Schematic diagram of three micro-processes in flotation. This figure is re-plotted according to Tao (2005).

The poor behavior of fine particles in bubble/particle attachment can also be reflected in the low recovery rate. It is experimentally evident that the recovery of the conventional flotation highly depends on the particle diameter (Parkinson and Ralston, 2011). The good recovery rate can be obtained from particle size range from 50 μm to 250 μm (Tao, 2004); however, it drops rapidly from the particle size 50 μm to about 10 μm (Feng and Aldrich, 1999). The low collection of fine particles could be explained by the small particle volume resulting in a lack of particle/bubble collision probability. Moreover, the fine particles are tendentious to be caught

in streamlines created by rising bubble, rather than to rupture the liquid film between bubble and particle (low P_c). (Zhou et al., 1997; Parkinson and Ralston, 2011).

As many minerals are finely disseminated throughout the ores, it has always been challenges to improve the recovery of fine particles. To increase bubble/particle collision probability, researchers have reported techniques such as oil-assisted flotation, carrier flotation, shear flocculation and selective polymer flocculation (Forbes, 2011; Warren, 1975; Trahar and Warren, 1976; Subrahmanyam and Frossberg, 1990; Gregory and Barany, 2011; Forbes et al., 2011) aiming to improve the effective size of fine particles through aggregation. The purpose of oil and carrier flotation is to aggregate fine particles with larger ones such as oil droplets or other hydrophobic materials. To overcome the repulsive energy barrier for particle/oil or particle/carrier attachment, strict physical and chemical condition requirements including high shear forces and proper pH range must be met. Also, the separation of oil/particle aggregation from water is a challenging task especially when oil emulsions are formed. On the other hand, the shear flocculation helps to achieve aggregation through applying a shear field with the aid of a collector, but it has the problem of high-energy consumption to produce adequate hydrodynamic conditions. Polymer flocculation is an efficient method to form aggregations by attaching particles onto the long chains, but the flocculants adsorption faces a challenge of low selectivity. Considering the disadvantages of the above techniques, the use of hydrodynamic cavitation in fine particle flotation is the focus of this thesis.

Hydrodynamic cavitation is a bubble generation method with good control of bubble size through adjusting the pressure, flow velocity and cavitation device geometry (Moholkar and Pandit, 1997; Gogate and Pandit, 2005). It shows a great potential to complement in the flotation process to increase the bubble-particle collision probability. Although the buoyant force

provided by the micro bubbles is not enough to float the particles, the presence of micro bubbles on the particles acts as bridges and greatly enhances the particle/flotation-sized-bubbles attachment probability (Rahman et al., 2014; Li et al., 2015). Besides the increase in the attachment probability, hydrodynamic cavitation also benefits the flotation process by forming the aggregation of fine particles, which increases the collision probability to the flotation size bubbles (Tao et al., 2008; Zhou et al., 1997).

Although the hydrodynamic cavitation has been experimentally proven to be effective in improving the fine particle recovery rate (Sobhy et al., 2013; Zhou et al., 2009), the mechanism of this process is still under study and requires further investigation. Venturi tube, as the most commonly used hydrodynamic cavitation device for mineral flotation applications, has shown its ability at affecting the local pressure and cavitation time scale through tuning the tube geometry (Arrojo and Benito, 2008). Hence the investigation on the Venturi tube geometry becomes promising for achieving higher bubble generation efficiency. On the other hand, particles with different wettability are often presented in the fluid under hydrodynamic cavitation especially in mineral flotation processes. The researches on the effect of particle properties on hydrodynamic cavitation behaviors would be a necessary step toward the fundamental understanding of underpinming science. Besides the particle properties, the dissolved gas and pre-existing bubbles in the system is also important for hydrodynamic cavitation. Their effects on hydrodynamic cavitation behaviors also need to be investigated.

1.2 Thesis objectives

In the Venturi tube geometry study, using both simulation and theory, I investigated the synergy between cavitation and Venturi tube geometry. Preliminary simulations allow us to narrow the key parameters regarding cavitation and power consumption. Systematic measurement of the pressure, velocity, cavitation inception and bubble generation were conducted for various Venturi designs. The loss due to the flow resistance (single-phase) was distinguished from the loss induced by the cavitation. The results reveal the key role played by the single-phase flow resistance (loss coefficient) on the cavitation inception and activity. Additionally, the bubble generation was correlated to the cavitation loss and the dissolved gas concentration. In the particle influence study, cavitation was performed with slurries containing particles with different properties at different concentrations. The effects of particle addition on cavitation were revealed by the change in the cavitation inception. The particle's critical property for affecting cavitation behavior was identified. Furthermore, the study on the effect of bubble injection on hydrodynamic cavitation were also performed.

1.3 Organization of the thesis

In Chapter 1, the use of hydrodynamic cavitation in mineral flotation and the tasks for this study is introduced. In Chapter 2, the advantages and disadvantages of cavitation, the geometry study of Venturi tube, mechanism of gas nucleation, and applications of hydrodynamic cavitation in water treatment, chemical reaction enhancing and food processing are reviewed. In Chapter 3, the simulation methods for the numerical study, and the material & methods for experimental study are specified for the investigation of Venturi tube geometry's influence on hydrodynamic

cavitation. The apparatus change and particle preparation for the particle and bubble addition study are also described in this Chapter. In Chapter 4 and 5, the numerical and experimental results for the Venturi tube geometry study and particle & bubble function study are presented and discussed. In Chapter 6, the results obtained in the last two Chapters are summarized, and their contributions to original knowledge are stated. In Chapter 7, future works regarding the hydrodynamic cavitation for fine particle flotation are proposed.

Chapter 2 Literature Review

2.1 Cavitation advantages of and disadvantages

The cavitation processes that have been utilized in various applications can be generally classified into two types: acoustic cavitation and hydrodynamic cavitation. If the process is triggered by the passage of high-frequency sound waves, it is called acoustic cavitation. Hydrodynamic cavitation is due to the pressure variation in the flowing liquid by the change in the geometry of the flowing system (Jyoti and Pandit, 2000). Despite the difference in starting mechanisms, both cavitation processes include the states of formation, growth, and collapse of microbubbles. The bursting of bubbles is accompanied by intense pressure waves, vigorous shearing forces, and localized heating. Without the proper control of the location and intensity, cavitation can behave as a destructive process to local materials. In the long history of cavitation study, it is at first regarded as a harmful subject to the hydraulic equipment (Karimi and Avellan, 1986; Singh et al., 2012; Hart and Whale, 2007; Shimizu and Yamaguchi, 1989). During the investigation of the equipment's erosion issue, the pump, compressor, and turbine that operate underwater are found to induce uncontrollably cavitation which causes a reduction of thrust and damage on components such as the impeller, turbine blade and equipment wall. The generation of hydrodynamic cavitation in these cases is due to the high rotating speed of the impeller, causing a rapid drop in the local pressure according to the Bernoulli's principle. Associated with high local pressure and temperature at the instant of collapse, the generated cavities eventually lead to the removal of elements of the material from the surface. In the operating conditions of the hydraulic machinery, cavities are repetitively formed, and the collapse of cavities generates shock waves that subject the material fatigue stresses (Hart and Whale, 2007).

Such damage has caused immeasurable loss to the offshore and hydropower industries, but also driven scientists to deeply investigate the mechanism behind this phenomenon.

As the investigations on its behavior were further carried out, cavitation due to its ability at bubble generation and violent energy releasing are gradually recognized as a helpful process in various applications. For example, cavitation has been intentionally generated for testing the intensity of erosion on various materials (A. Karimi and Avellan, 1986; Shimizu and Yamaguchi, 1989). The acoustic cavitation also shows its ability in cleaning the containments on material surfaces (Krefting et al., 200). As the potential of interaction between bubble and ultrasonic force field is gradually realized, more and more researches have been carried out to implement cavitation in more advanced applications. For instance, the ultrasonic-generated acoustic cavitation can be used to contribute to the modern healthcare. As it is difficult to control the therapeutics to several portals of the human body, acoustic cavitation provides a feasible solution as the lipid tissue is permeable to acoustic waves, and the cavitation activity can be remotely incited in the diseased tissue for applications such as drug delivery. (Paliwal and Mitragotri, 2006; Crake et al., 2016).

2.2 Applications of cavitation

Besides the use of cavitation in mineral processing and bio-medical field, due to its energy efficiency and simplicity (Gogate, 2009), it recently raised interest in various industry-scale applications. By understanding the use of cavitation in those areas, the utilization of acoustic or hydrodynamic cavitation can be adjusted accordingly to optimize the benefit for each processes.

2.2.1 Water treatment

Cavitation has been utilized in the water treatment industry for its ability to efficiently generate bubbles. The bubbles at the instant of burst release high magnitude energy, which can physically and chemically destroy microorganisms and disinfect wastewater. (Arrojjo et al., 2008; Dular et al., 2016; Jyoti and Pandit, 2000). Comparing to the traditional water disinfection with chemical additives, cavitation does not result in the formation of any toxic byproducts. It is also economical and efficient in terms of large-scale water treatment scheme. To have the hydrodynamic cavitation as the pretreatment, the consumption of chemical additives for killing microbes can be substantially lowered (Jyoti and Pandit, 2000).

Like the acoustic cavitation which is triggered by the oscillating ultrasonic field, hydrodynamic cavitation is driven by the sudden drop and recover in pressure due to change in flow velocity (Dular et al., 2016). The rapid change in the surrounding environment results in the generation of oscillating bubbles. By adjusting the ultrasonic field or pressure recovering time (different frequencies), cavitation can manifest itself in different properties and mechanisms for implementing into different scenarios. High frequencies generate a higher number of collapse and promote the diffusion OH^- radicals, which can be used as a biocide in water treatment, but the generated bubbles are less energetic. On the other hand, low frequencies tend to generate more violent collapse and strong shock waves but at the expense of less collapse per unit time and less diffusion of OH^- radicals (Arrojjo et al., 2008).

Comparing to the acoustic cavitation, which disinfects water mostly by chemical processes with generation of OH^- radicals, mechanical disruption of bacteria plays a major role in hydrodynamic cavitation. The bacteria tends to form clusters and the external microorganisms can act as protection against biocides. The shear force produced by cavitation can break the

agglomerates and isolate the individual bacteria, which increases the efficiency of biocides (Joyce et al., 2003). Therefore, the disinfection rates are maximized by those configurations that promote large bubbles and higher cavitation activities (Arrojjo and Benito, 2008).

The efficiency of using orifice plates in rhodamine B degradation is also compared with the results of using acoustic cavitation. The hydrodynamic cavitation using orifice plates were proved to produce higher disinfection rate, with a higher energy efficiency than the acoustic cavitation. Moreover, the scale up of the hydrodynamic cavitation reactors is easier as having a constriction in the flow system is readily available. (Parag R. 2010, Manickam 2001). Overall, hydrodynamic cavitation is a relatively simple and energy efficient technology that is promising to be implemented on an industrial scale of water treatment.

2.2.2 Chemical reaction enhancing

In the conventional chemical processes such as chemical synthesis with oxidation reaction, the utilization of acoustic cavitation has been extensively studied (Pinjari and Pandit, 2011; Jitendra, 2016). However, due to poor transmission of acoustic energy in the large volume of water and low energy efficiency, the implement of acoustic cavitation in industrial scale processes has been a challenging task (Gogate and Pandit 2004). The researchers recently highlighted the use of hydrodynamic cavitation in the chemical processes. Despite the disadvantages of less intense collapse compared to the acoustic cavitation, hydrodynamic cavitation has the advantages of easy scaling up and high energy efficiency.

For a better description of cavitation's effect in chemical processes, the collapse of cavities can be classified into two types: symmetric and asymmetric (Mahulkar and Pandit, 2010). The symmetric collapse happens when the cavity remains spherical until burst that forms reactive free radicals favoring thermal pyrolysis of organic molecules. For the asymmetric collapse, the

collapsing cavity is not spherical because of the presence of wall or particle at the point of collapse. It produces high-velocity liquid jets and intense local turbulence, which is favorable for physical transmission. In the symmetrical collapse condition, when the water is under cavitating conditions, the highly reactive hydroxyl radicals (OH^-) are formed from the dissociation of water molecules. The symmetrical collapse is beneficial especially for the oxidation reactions that are primarily induced by the formation of reactive free radicals. The oxidation processes caused by cavitation happens in two ways: First, the molecules trapped inside of the cavity undergo thermal decomposition during the collapse. Second, the formed radicals attach the targeted molecules at the cavity liquid interface and in the bulk liquid thereby oxidizing the molecules (Saharan et al., 2013; Jitendra, 2016). During the cavitation, each cavity behaves as a micro-reactor, which releases a large amount of energy and create a local condition of high pressure and temperature (Yusuf and Adewuyi, 2001).

Pandit and Joshi first tested the use of hydrodynamic cavitation in the hydrolysis of oils in 1993. The experiment showed an improved hydrolysis yield with the use of HC. The traditional hydrolysis methods require high temperature and pressure, as well as the high interfacial area between the catalyst and the oil. With hydrodynamic cavitation, spots with adequate temperature and pressure can be created at many locations inside the reactor. Also, the size of the catalyst emulsion is mechanically reduced, which facilitates better interaction between the oil and catalyst (Jitendra, 2016). In the same manner, hydrodynamic cavitation was shown to be helpful in the crude oil upgradations, for its ability at producing high temperature, pressure, and catalyst-reagent contact area to break large molecular petroleum fraction into the smaller fractions (Ansari et al., 2015; Jitendra, 2016).

2.2.3 Food Processing

The traditional heat-treat process for food sterilization involves several problems including low efficiency at killing heat-resistant microorganisms, high energy consumption and risks in destroys heat labile nutrients and flavor components. Inspired by the contribution in water treatment industry, cavitation is regarded as an alternative method for commercial sterilization of food by the processors (Milly et al., 2007; Gogate, 2011; Bhaskaracharya et al., 2009). By using the hydrodynamic cavitation without any further processes, the induced destructive forces can effectively inactive cells of bacteria, yeast, and heat-resistant bacterial spores, and the microbial lethality induced by hydrodynamic cavitation is reported to be greater than that accounted by thermal effects. To combine the hydrodynamic cavitation with traditional heat treat process, the lethality of common spoilage microorganisms can be achieved at reduced temperature due to the synergistic effect of cavitation and temperature. This way, the heat labile components can be retained, and foods such as fruit juice, salad dressing, and milk can be safely processed.

Besides of food sterilization, cavitation can be beneficial for many other applications in the food processing industry. The ultrasonic induced acoustic cavitation has been developed to accelerate processes such as freezing, thawing, crystallization of lactose, and to improve processes such as cutting, extraction, emulsification, and aging of wines (Mawson and Knoerzer, 2007; Bhaskaracharya et al., 2009). Considering the energy efficiency in food processing which involves large volumes, hydrodynamic cavitation is suggested to be the alternative to acoustic cavitation. It has shown promising potential at solving many problems faced by the food industry such as the replenishment of moist lost during the storage and primary processing (Ashokkumar et al. 2011). In the hydration process, hydrodynamic cavitation can assistant

chemically pure protein to bind theoretically up to 40% water by weight. The formed hydration shells of protein increase their affinity for water during the precipitation. In addition, the formation of dense and strong hydration shells raises the thermal resistances of the dissolved valuable nutrients and vitamins, preventing them from thermal denaturation at the subsequent heat treatment.

2.3 Cavitation device geometry effect

Hydrodynamic cavitation can be generated by the passage of liquid through devices with constricted area. The orifice plate and Venturi tubes, as two most common hydrodynamic cavitation devices, have similar, yet different geometric structures. To study the influence of geometry on hydrodynamic cavitation, the two devices have drawn researchers' interests and their potential in various applications were compared (Arrojo, 2008; Gogate, 2005; Saharan, 2013). As discussed in the water treatment study, cavitation destroys microorganism through both chemical (generation of OH^- radicals) and mechanical (shear forces and de-clumping effect) processes. Venturi tubes surpass orifice plates in disinfection rate with an outstanding mechanical effect since it shows a better performance in de-clumping bacteria agglomerates and tends to give denser cavitation cloud and a larger number of cavitation events. Also, the flow rate in the Venturi tubes is higher than that of orifice plates at a given power input, leading to a higher treatment capacity and better energy efficiency. On the other hand, the orifice plates have a larger localized pressure intensity immediately after the device, and the disinfection effect from orifice plates is partially related to the OH^- generation, while the chemical effect is almost negligible with Venturi tube (Arrojo, 2008). The same comparison was also performed on the degradation of dye as a model pollute (Saharan, 2013). In the study, Venturi tubes again

outperformed the orifice plate owing to the higher degradation efficiency and energy efficiency. Saharan et al. suggest that the effect of HC on degradation depends on the number and maximum sizes of cavities. In the case of Venturi tubes, the pressure recovers smoothly due to the divergent angle, leaving the cavities enough time to grow to maximum size, whereas the pressure recovers immediately after the orifice plates and the cavities collapse before reaching maximum size, thereby reducing the collapse intensity and cavitation yield. In conclusion, the orifice plates are favorable for intense chemical reactions and milder processes. While the use of Venturi tubes are more energy efficient, and suitable for the producing physical effects (Gogate, 2005; 2009).

In the case of orifice configuration study, the cavitation intensity can be controlled by changing the orifice to pipe diameter (free area) ratio, as well as the number and diameter of the orifice holes (Gogate, 2000). The cavity collapse pressure was found to decrease with the increase of free area ratio because larger flow area leads to a lower orifice velocity, resulting in a slower cavitation inception and fewer activities. If the free area and inlet pressure are kept constant, the cavity collapse pressure increases with the increase in hole diameters. The cavitation inception also happens faster with bigger hole diameter, which results in a greater extent of cavitation for the same orifice velocity (Yan and Thorpe, 1990; Gogate, 2000). The effect of orifice plates' geometry on cavitation properties has been experimentally investigated in water treatment process (Gogate, 2010). As shown in Figure 2-1, among the tested plates, plate 1 exhibits more cavitation yield and higher degradation rate of rhodamine B with less energy supplied. For the plates having the same flow area, smaller hole sizes result in a higher pressure fluctuation frequency and larger area of shear layer (Manickam 2001).

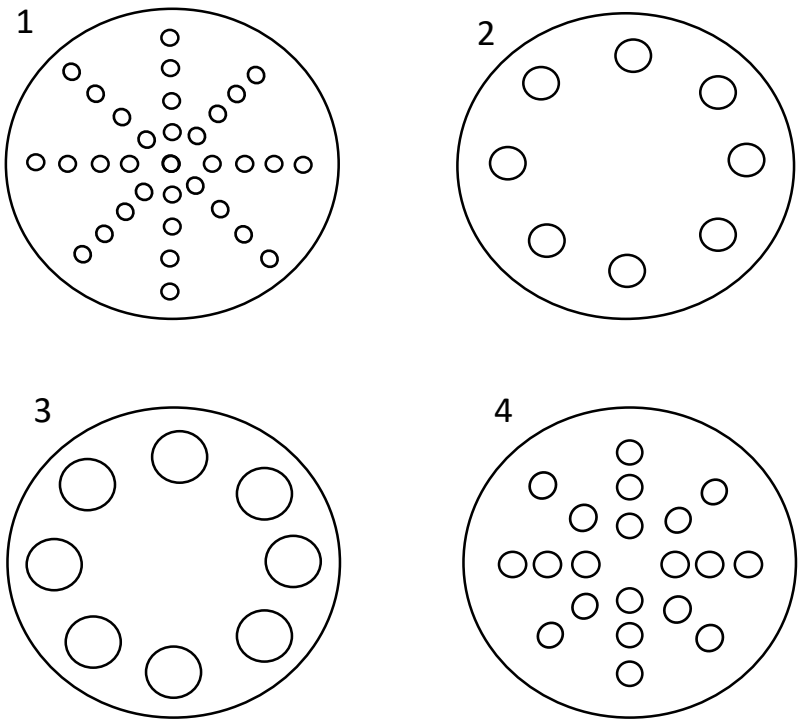

Figure 2-1. Multiple-hole orifice plates having different combinations of number and size of holes for water disinfection efficiency study. This is replotted according to Sivakumar (2002).

The geometrical parameters of a Venturi tube have also drawn some researcher's attention as they can significantly impact local pressures and cavitation time scale (Arrojo and Benito, 2008). With the advantages of easy monitoring as well as geometry and ambient condition control, CFD simulation was widely used in the parameter study (Agarwal, 2011). Increasing tube throat length has been shown to have no noticeable effect on tube losses and pressure changes except increasing the cavity size (Sivakumar and Pandit, 2002; Arrojo et al., 2008, Dular et al., 2016). Increasing outlet-throat diameter ratio enlarges pressure difference at the same flow rate (Sivakumar and Pandit, 2002; Arrojo et al., 2008). When outlet angle increases, the pressure difference at inception decreases and the vapor generation amount increases together with the

intensity of collapse, causing unsteady flow rate (Dular et al., 2016; Ashokkumar et al., 2011; Gogate, 2011). To complete the Venturi parameter research, the cavitation behaviors need to be examined. Dimensionless numbers such as cavitation number and loss coefficient are efficient tools to globally describe the flow behavior as well as indicating the cavitation inception (Milly et al., 2007).

2.4 Gas nucleation by cavitation

The gas nucleation in water can be achieved by roughly two processes. One is to raise the temperature above the saturated vapor/liquid temperature, such as boiling. The other is to drop the pressure below the vapor pressure, usually caused by hydrodynamic cavitation (Christopher et al., 1995). According to Henry's law, the amount of dissolved gas in solution is proportional to the gas pressure at a constant temperature. In the case of hydrodynamic cavitation, liquid pressure is experiencing a sudden drop at the constriction area causing a corresponding increase in the gas saturation concentration. Once the pressure drops below the vapor pressure, gas molecules tend to be released from the liquid phase. The driving force can be quantified by the pressure difference, ΔP, between vapor pressure and liquid pressure. In some literatures, it also represents a level of super-saturation or tensile strength (Jones, 1999; Sukep and Or, 2005). To generate a gas bubble of a certain size, energy has to be consumed to create the bubble and overcome the negative pressure over the bubble area. Consequently, for a given liquid-gas surface tension (γ_{LV}) and ΔP, a critical bubble radius must be reached to overcome the energy barrier for the bubble to grow. As shown in Figure 2-2, a bubble with a radius smaller than the critical radius tends to condense because it is more energetically favorable. Once the energy barrier is overcome, the bubble will grow spontaneously.

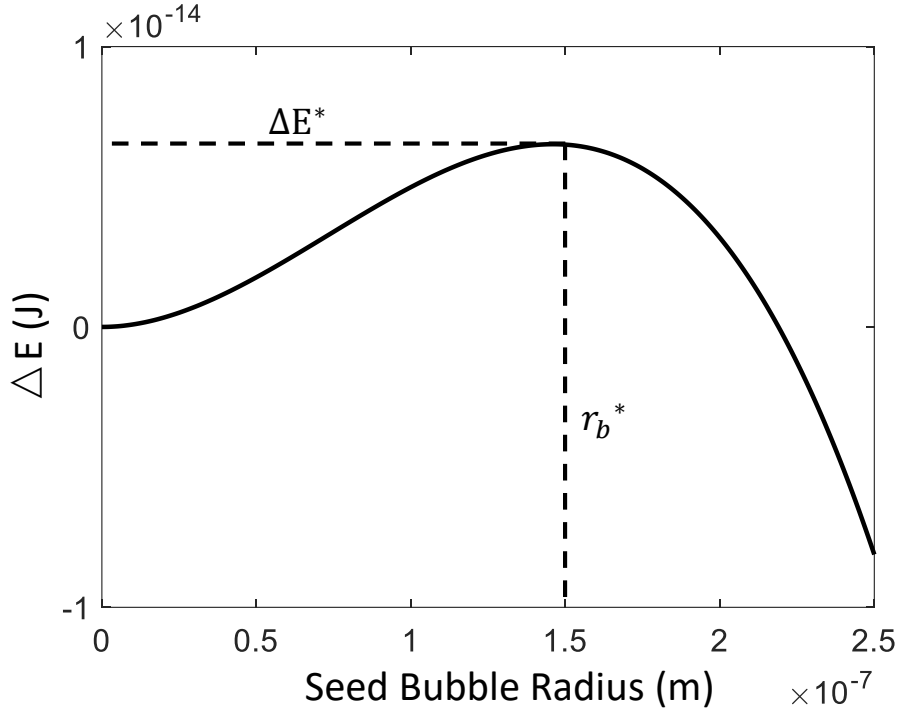

Figure 2-2. Bubble nucleation energy as a function of seed bubble radius for ΔP = 1 MPa. $\Delta E^*$and $r_b{}^*$ are the nucleation energy barrier and critical bubble radius respectively.

Based on the differences in nucleation sites, the conventional nucleation can be classified into two categories: homogenous nucleation and heterogeneous nucleation. Homogeneous nucleation is the formation of gas nuclei in the bulk of the pure liquid and requires a high level of super-saturation. The water-air surface tension γ_{LV} is about 73 mN/m in 20 ºC. To generate a bubble with radius $r_b = 2\gamma_{LV}/\Delta P$, the required energy consists two parts: the bubble surface energy, $4\pi r_b^2 \gamma_{LV}$, and the work to displace liquid, $\frac{4}{3}\pi r_b^3 \Delta P$. By combining the two energy expression with the Laplace equation, the energy barrier to generate a bubble is obtained (Caupin and Herbert, 2006; Christopher et al., 1995), and defined as:

$$E_b = \frac{16\pi}{3}\frac{\gamma_{LV}^3}{\Delta P^2} \tag{2.1}$$

In practical engineering circumstances, achieving homogenous cavitation is difficult. Cavities tend to be formed on the nucleation sites such as the wall of the liquid container, or the surface of suspending particles. This is termed heterogeneous cavitation. The formation of a bubble on a smooth solid surface with the same radius in homogeneous nucleation requires lower energy because of wetting (Caupin and Herbert, 2006; Zang 2015). The energy barrier is defined as:

$$E_b = \frac{16\pi}{3}\frac{\gamma_{LV}^3}{\Delta P^2}\frac{(2-cos\theta)(1+cos\theta)^2}{4} \tag{2.2}$$

Where θ is the contact angle of liquid on the solid surface. In theory, the bubble formation on an extremely hydrophilic solid with $\theta = 0^o$ requires as much energy as that for the homogeneous nucleation. On the other hand, the presence of a hydrophobic surface would strongly reduce the energy barrier because the increase in θ reduces E_b, and no energy would be required if θ approaches π. Based on the above examination, heterogeneous nucleation becomes more favorable with the increase in the solid hydrophobicity. This theory can be visually illustrated by Figure 2-3 case (a) and (b). As the bubble tends to be stretched flat on the hydrophobic surface, the formation of a bubble with same volume is associated with higher radius on a hydrophobic surface, thus it is easier to reach the critical bubble radius compared to the case on the hydrophilic surface. At the microscopic scale, crevices are distributed on the solid surfaces, and the effects of surface geometries need to be considered. A conical crevice geometry as shown in Figure 2-3 case (c) is commonly used to study the effect of surface geometry (Christopher et al., 1995; Apfel, 1970; Jones, 1999). The volume of the cavity in the meniscus, depending on only θ and the groove angle, 2α, is smaller comparing to that with a same radius on a flat surface, thereby requiring less energy to form. However, as the bubble emerges at the

cavity mouth, the radius of the cavity decreases, e.g. from R1 to R2, before increasing again. Without the support from local fluctuation, the further emerge of cavity becomes difficult because the required tensile strength increases. If the cavity successfully emerges from the crevice, the radius would increase again. This process is easier with a hydrophobic surface.

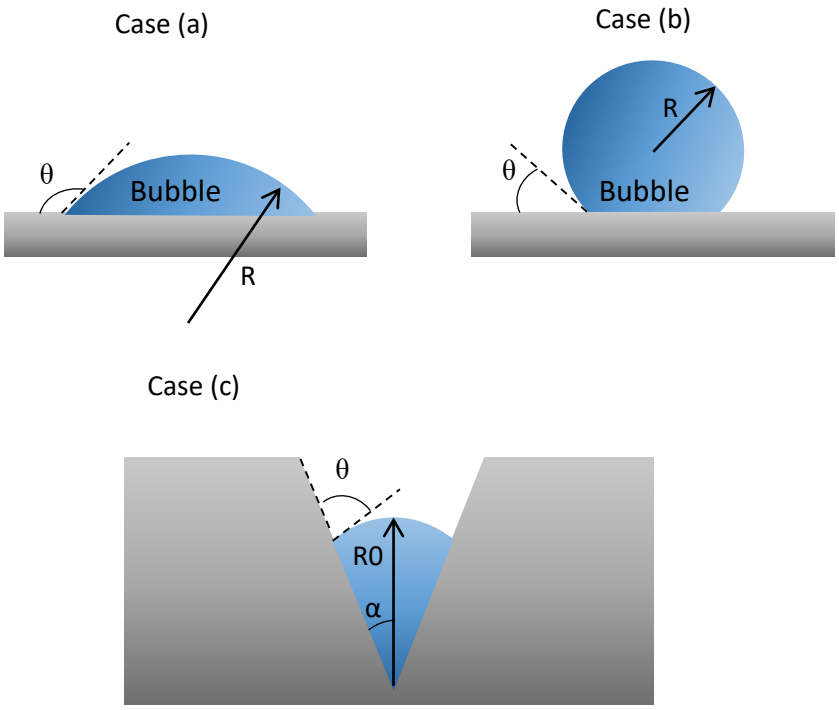

Figure 2-3. Three models of heterogeneous nucleation. (a) Flat hydrophobic surface ($\theta > \pi/2$). (b) Flat hydrophilic surface ($\theta < \pi/2$). (c) Conical cavity. This figure is replotted according to Christopher et al. (1995) and Jones (1999).

The homogeneous and heterogeneous nucleation discussed above are categorized as the conventional types of nucleation. In practical circumstances, nucleation rates are mostly higher than the theoretical value. This is due to the presence of dissolved gas and pre-existing bubble nuclei (Brennen, 1995; Jones, 1999; Caupin and Herbert, 2006). If a nucleation bubble contains gas content, the gas partial pressure p_g would contribute to the pressure in the bubble, and the

critical tensile strength would become 2 $\gamma_{LV}/r_b - p_g$. As the concentration of dissolved gas increases, the tensile strength decreases to zero or even negative value, resulting in the spontaneous growth of bubble at the liquid pressure greater than the vapor pressure. The pre-existing bubble nuclei, on the other hand, reduce the nucleation energy required to overcome the barrier for bubble growth. Experiments have been performed to demonstrate the effect of bubble nuclei on bubble generation (Bremond et al., 2006). Acoustic energy was applied to a hydrophobic plate under water. With the micro-cavities etched on the solid surface, cavitation was found to be promoted at higher pressure.

Chapter 3 Experimental Setup and Procedures

3.1 CFD Simulation

The preliminary single phase simulations were performed to model the hydrodynamic condition inside the Venturi tubes. Although the preliminary simulation results cannot predict the condition of hydrodynamic cavitation, the results can help narrow down the critical parameters for experimental investigation by indicating those having large impact on tube pressure profile. A computational fluid dynamic (CFD) commercial software (COMSOL Multiphysics Version 5.1) was used to carry out the liquid phase simulation. The liquid flow was simulated using a stationary condition and k-ω turbulence model because it is more accurate in simulating the internal turbulent flow comparing to the k- ε model (Eiamsa et al., 2009). The default values of k-ω turbulence model parameters provided in COMSOL were used to perform the simulation. Figure 3-1 shows the steps of the single-phase geometry simulation study. First, the geometry models with parameters listed in Table 3-1 are constructed in a 2-D axisymmetric domain, aiming to investigate the tube inner pressure change affected by the four main parameters as shown in Figure 3-2: the convergent or inlet angle (α), the throat length (L), the divergent or outlet angle (β) and the diameter ratio (D/d). For all the geometries, the inlet and outlet diameters were kept constant at 9 mm to match the hose size in the experimental study. Sensitivity tests were performed for different mesh sizes and the velocity and pressure results were found to converge at the level of "finer mesh" with a minimum number of 100,000 elements. This level of mesh fineness was used so that simulation errors introduced by mesh size can be minimized. The majority of the elements are triangular and located in the tube center

area for a fast simulation speed. Five layers of quadrilateral elements were stacked inside the edge of the tube wall for a better accuracy of wall function. The step after constructing the 2D geometry is to set the boundary conditions at the pre-simulation stage. To be consistent with the experimental condition, the pressure at the outlet was fixed to one atmosphere. The inlet velocity was varied to achieve throat velocities consistent at 20 m/s for different geometries. After the simulation was completed, pressure profile is extracted along the center of the tube. The differences in pressure profile with different geometries are compared to give preliminary results of effects of parameters on cavitation.

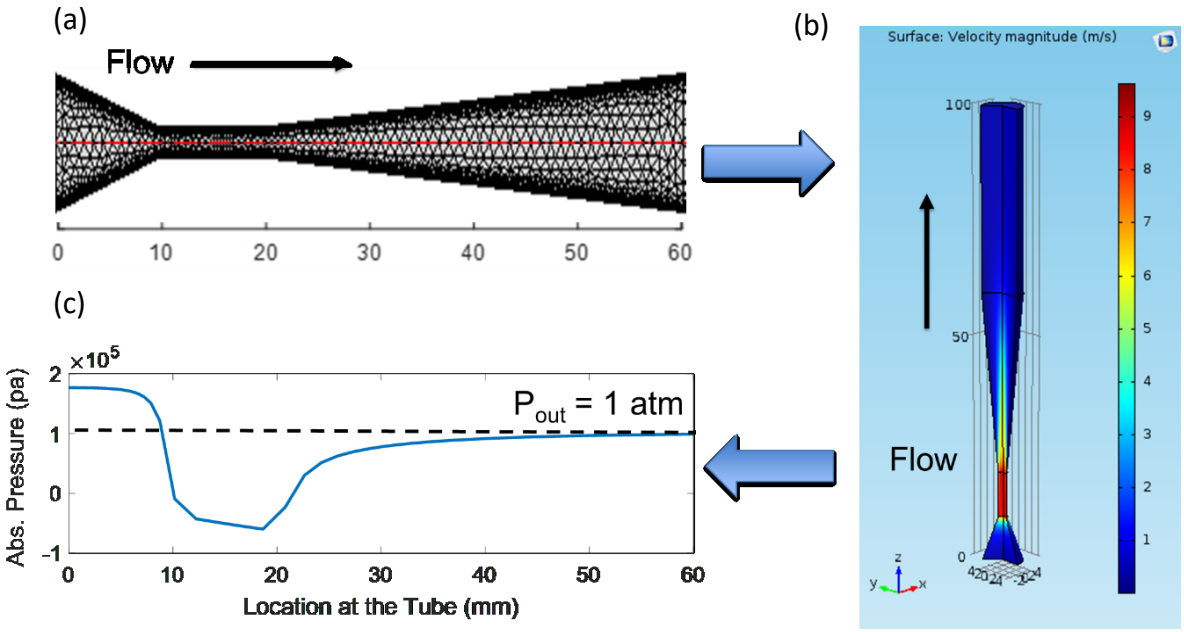

Figure 3-1. Three steps of single-phase simulation study: (a) construction of tube geometry, (b) simulation performance, (c) extraction of pressure profile.

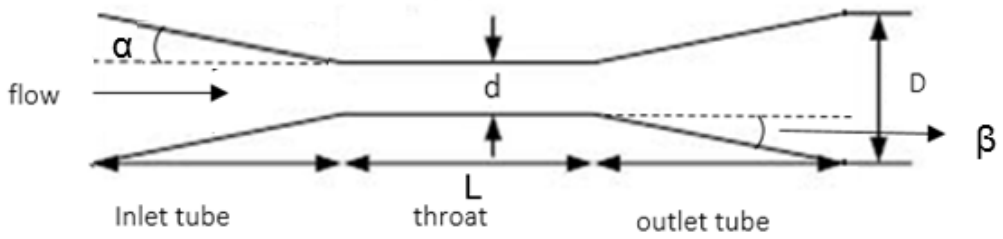

Figure 3-2. Schematic diagram of a Venturi tube and its associated parameter symbols.

Table 3-1. Specifications of Venturi tubes tested in single-phase numerical simulation.

Subject	Inlet Angle, α (°)	Throat Length, L (mm)	Inlet Diameter, D (mm)	Throat Diameter, d (mm)	Outlet Angle, β (°)	Diameter Ratio, D/d
Inlet Angle	5	10	9	2	5	4.5
Inlet Angle	12	10	9	2	5	4.5
Inlet Angle	19	10	9	2	5	4.5
Inlet Angle	45	10	9	2	5	4.5
Throat Length	19	5	9	2	5	4.5
Throat Length	19	10	9	2	5	4.5
Throat Length	19	20	9	2	5	4.5
Outlet Angle	19	10	9	2	5	4.5
Outlet Angle	19	10	9	2	12	4.5
Outlet Angle	19	10	9	2	19	4.5
Outlet Angle	19	10	9	2	90	4.5
Diameter Ratio	19	10	9	4.5	5	2
Diameter Ratio	19	10	9	2.6	5	3.5
Diameter Ratio	19	10	9	2	5	4.5
Diameter Ratio	19	10	9	1.5	5	6

3.2 3D printing

Although 3D printing technology was first invented in the 1980s (Bose et al., 2013), through the improvements made in speed and quality it has recently become more popular for many applications including engineering, research, manufacturing and medical industries. This technology has the advantage of fast production of specially designed products without the need for specific tooling. In the experimental study on Venturi tube geometry optimization there was need of many Venturi tubes with different geometries to be created, for which I used 3D printing

in this study. To construct a 3D object, the first step is to build the 3D model of the desired Venturi tube by using computer-aided design software (CAD) as shown in Figure 3-3. The 3D model file is then loaded to the corresponding 3D printers for the print. The tubes were first printed by using a traditional printer with the direct PLA writing technology where the object is fabricated layer over layer by deposition of strands. As shown in Figure 3-4, the direct writing printed tube on the left is porous with rough surfaces, which is not desired in the pressurized cavitation condition. The Autodesk Ember Printer equipped with Stereolithography (SLA) technology, as one of the most accurate forms of 3D printing, becomes the final choice. SLA works by solidifying the liquid resin with light and builds objects layer by layer. It has the advantages of printing products with relatively strong structures and high surface smoothness (Lee et al. 2016; Tumbleston et al., 2015).

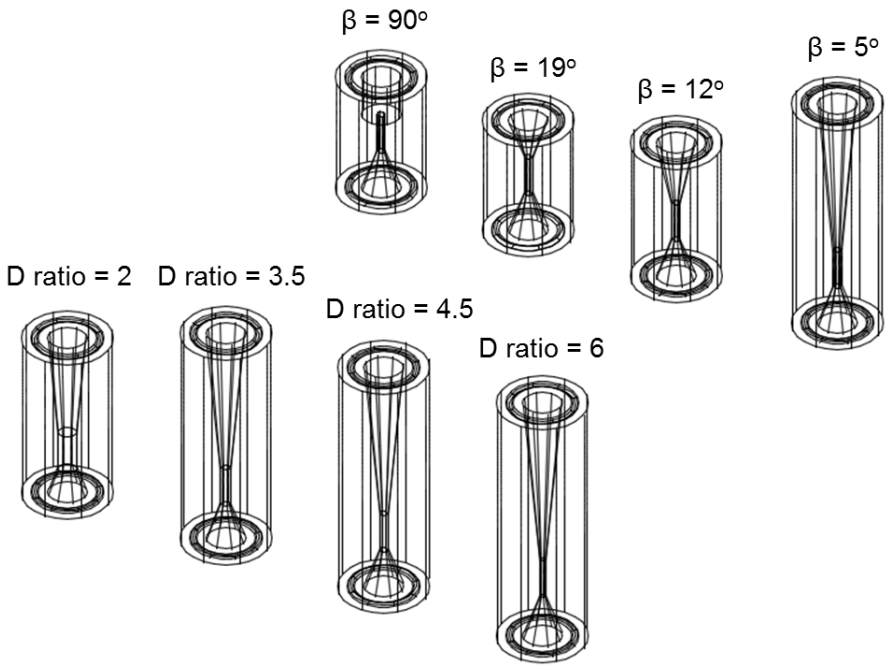

Figure 3-3. 3D models of Venturi tubes used for geometry investigation.

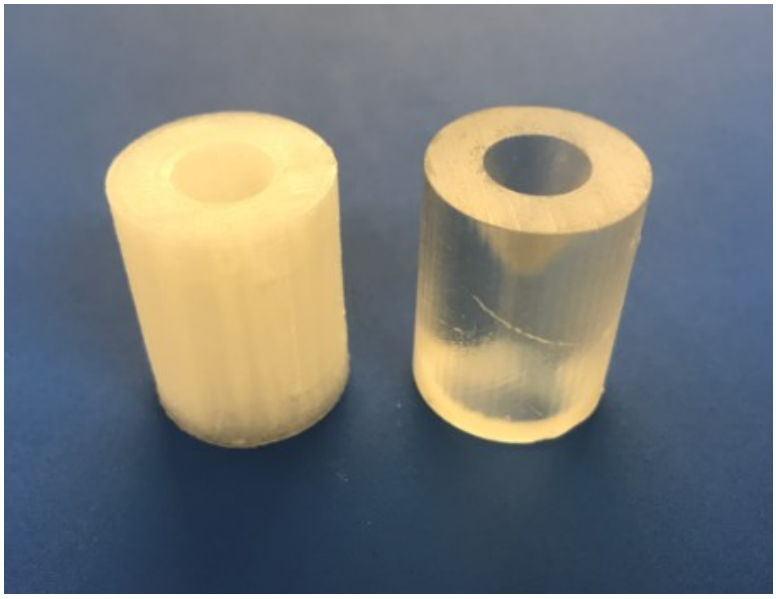

Figure 3-4. Tube product printed by using the direct ink writing (left) and SLA (right).

3.3 Equipment setup

3.3.1 General material and equipment

Figure 3-5 shows the experimental setup used in Venturi tube geometry study. Tap water was pumped through the circuit by a peristaltic pump (Masterflex I/P Easy-Load) which can deliver a flow rate ranging from 0 to 10 L/min. The pump discharged pulsating flow that is dampened using a sealed tank with design pressure of 300 kPa. The inlet pressure (p_u) was measured by using a pressure transducer (IKA RW 20 digital) which sends pressure information in voltage signal to an oscilloscope (Rigol DS1054Z) through a coaxial wire connection. The outlet pressure was found to be constant and equal to the atmospheric pressure.

The flow rate (Q) was measured with an Omega FLR1001 type flow meter. It is equipped with a turbine wheel that rotates at different rates in response to the liquid flow. Infrared light energy is emitted to the turbine wheel, and is alternatively reflected and absorbed from the black and white spokes evenly deposited on wheel surface. The electrical pulses generated by light sensor

reflect liquid flow rate, and is simultaneously displayed on the oscilloscope through connection. The measurements were taken once a stable state was reached (steady pressure and flow rate).

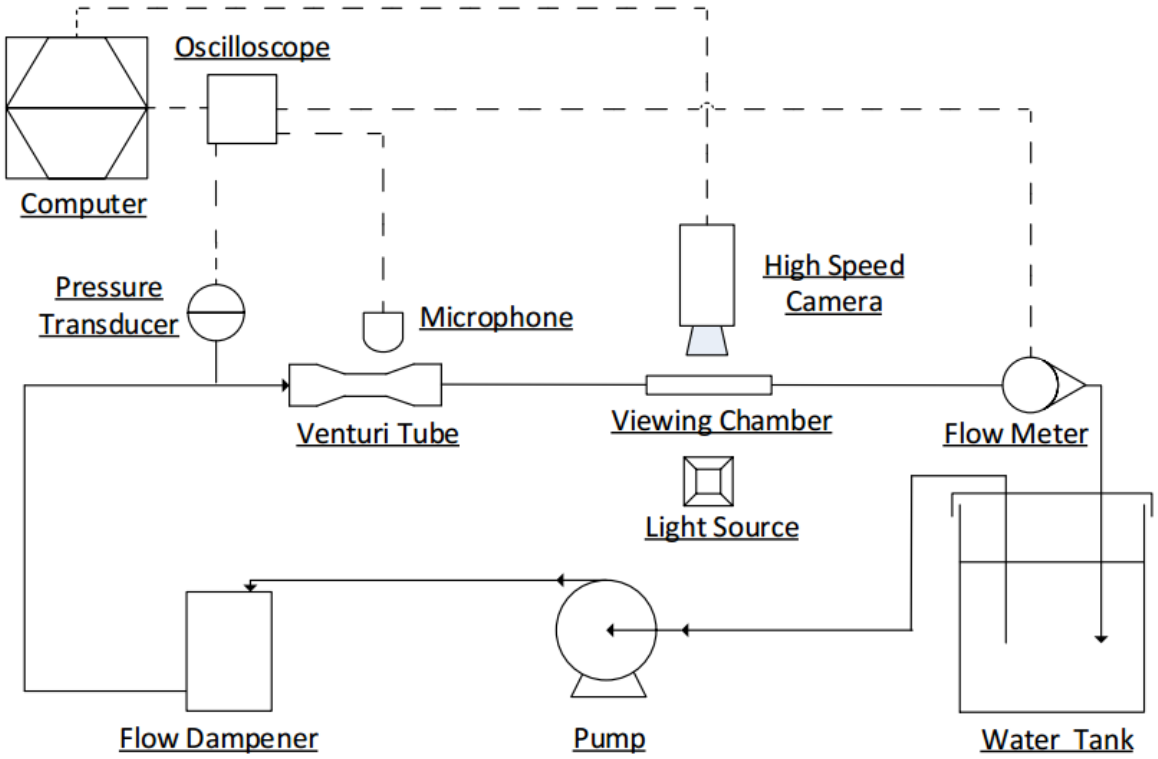

Figure 3-5. Schematic of the experimental setup using in Venturi tube geometry study.

3.3.2 Cavitation inception measurement

A high-performance microphone (Florida Research Instrument 100-1) was used to measure the cavitation inception. The microphone was connected to the oscilloscope and placed 1cm above the end of the Venturi tube constriction (Figure 3-5). When cavitation occurs, bubbles collapse and radiates high frequency energy waves which are detected by the microphone. To measure the cavitation inception the flow rate was gradually increased while the oscilloscope is recording. 24 seconds of audio at a sampling rate of 500k sample/s was recorded for each loop. The measured audio waves were transferred to the computer where they were processed and presented in the form of power spectral (Figure 3-6) by using Welch's power spectral density estimate in MATLAB. This function rearranges the acoustic waves by the frequencies and replotted the data in the form of normalized intensity power against frequency. The cavitation inception, v_{inc}, is characterized as the speed when the power spectral starts to deviate from the baseline, which is recorded before cavitation inception.

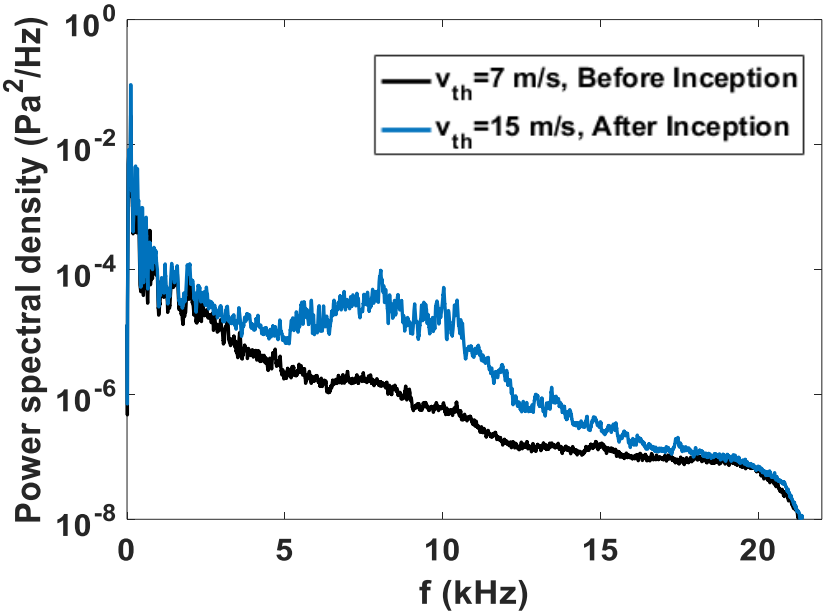

Figure 3-6. Acoustic power spectrum of two different throat velocities before and after cavitation inception.

3.3.3 Bubble generation measurement

The number of bubbles generated by hydrodynamic cavitation was monitored using a high-speed camera at 125 fps equipped with a high magnification lens. The observation is proceeded through a glass-viewing chamber placed 26 cm downstream from the Venturi tube (Figure 3-5). The viewing chamber has a flat wall facing the camera to avoid the distortion of the images. A light source is illuminating from the back of the chamber to provide enough light intensity for clear imaging. As shown in Figure 3-7 (a), a MATLAB image analysis code was used to detect in-focus bubbles and measure bubble size. Figure 3-7(b) shows an example of the bubble size distribution that was calculated using 1362 images.

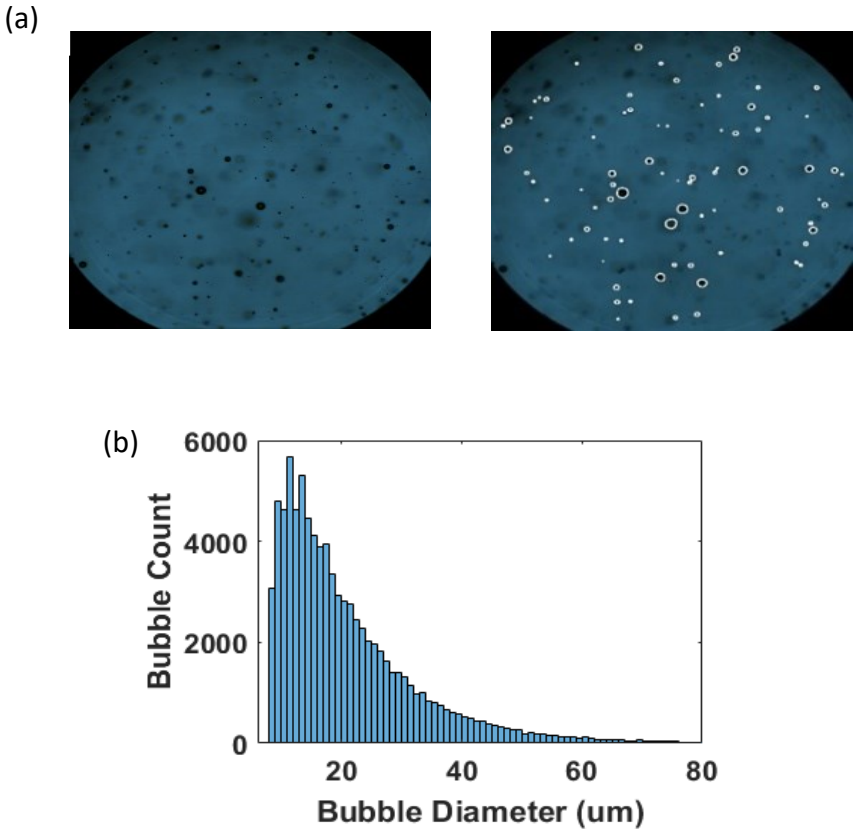

Figure 3-7. (a) High speed camera image and the recognized bubbles in white circles. (b) Bubble size distribution calculated based on the images.

3.3.4 Flow damper and dissolved gas

A sealed tank filled with water and air was used to dampen the pump pulsations (Figure 3-5). As the pulsating flow enter the dampener from the top, the air, being a compressible fluid, smoothed the fluctuations. The pressure inside the dampener is built up with higher flow rate. According to Henry's law, more air tends to be dissolved in the water with higher pressure. In the geometry study, the amount of dissolved gas was kept constant by insulating the air inside balloons (no air-water interface). The influence of dissolved gas was studied by removing the balloons, which allowed the air to dissolve in water as the inlet pressure increased.

3.3.5 Setup adjustment for particle addition and gas injection

The experimental set up was partially adjusted for the study of particle addition on cavitation behavior as shown in Figure 3-8. The water tank was replaced with a mixing tank for a better particle-water mixing. An impeller driven by an adjustable agitator is used to provide mixing forces to the slurry. The rotating speed of the impeller was set at 500 rpm for mixing hydrophilic particles. A higher stirring rate of 900 rpm was set to mix the hydrophobic-treated particles because extra shear force was required to break the aggregations that they naturally formed inside water. A visual inspection was performed through the translucent tank wall before each run to ensure the good mixing of particles. A smaller size flow dampener filled with water and an air balloon was used so that the water and particle usage amount could be reduced, and the gas-dissolving problem at pressurized tank was further minimized. The flow meter was relocated to the upstream of the pressure transducer to avoid the pressure increase induced by the resistance from the flow meter. Calibration on flow meter was performed before each particle run in order to minimize the effect of particle blockage on infrared light transmission.

Due to the mechanism of the flow meter, it is not able to deliver accurate flow rate in the conditions with dark particles such as graphite and molybdenite, or high concentrations of translucent particles such as silica and glass beads.

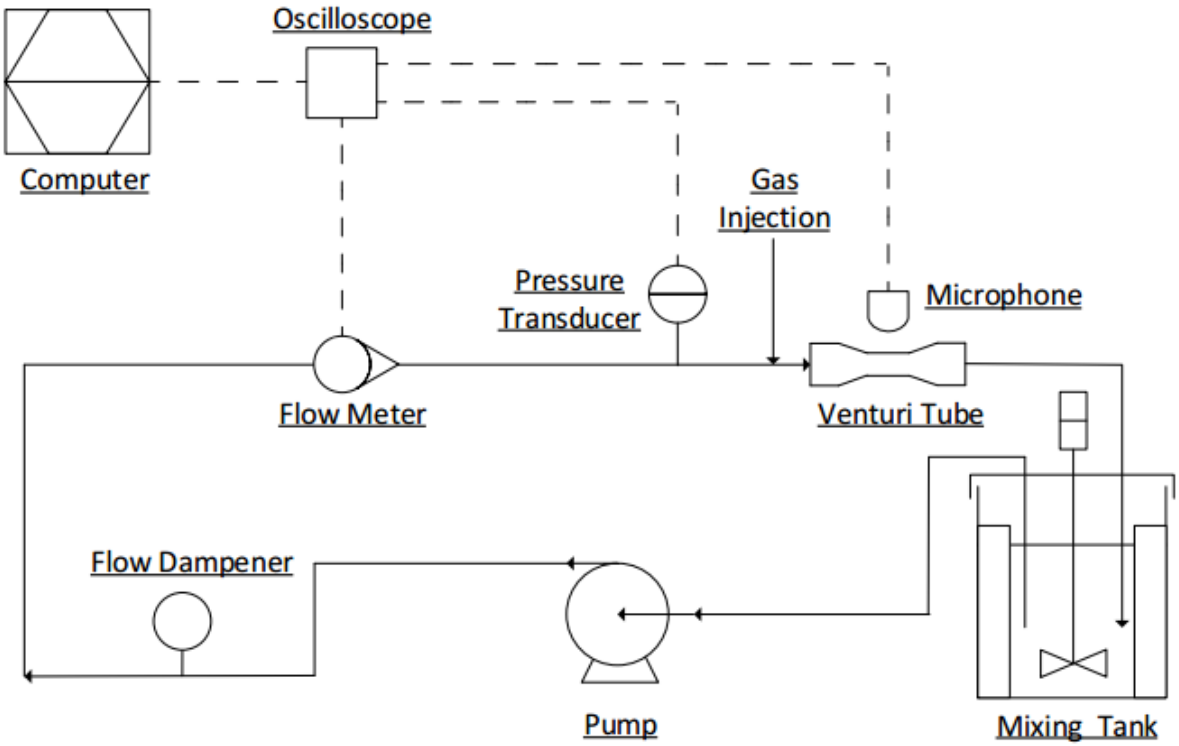

Figure 3-8. Schematic of the experimental setup used in the particle and bubble addition study.

In the study of bubble injection effect, a stainless steel Venturi tube holder with inlet gas injection site was used as shown in Figure 3-9. The 3D printed inner core with Venturi geometry can be inserted to the central part. Two side parts with the same diameter to the hoses were applied to clamp the tube from the both two sides. A gas injection site was located at 5 cm upstream of the Venturi tube. For breaking the injected air into smaller size bubbles, a mesh wire was placed at the exit of the gas hose.

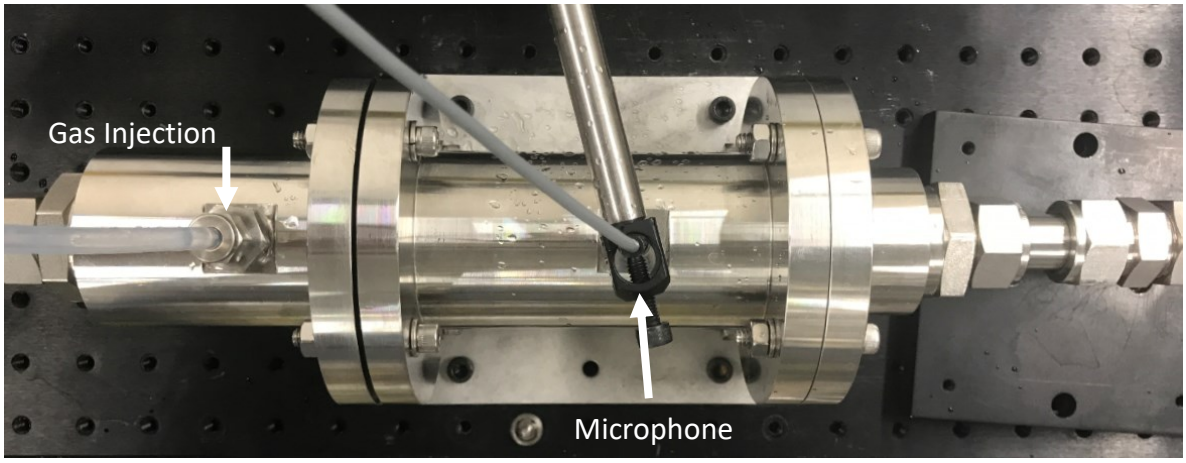

Figure 3-9. Picture of the Venturi tube holder with gas injection at tube inlet.

3.4 Parameters and equations

The power consumption P, to drive the flow across the Venturi tube, was calculated using:

$$P = Q \times (p_u - p_d) \tag{3.1}$$

where p_d is the downstream or outlet pressure, and p_u is the upstream or inlet pressure.

The conventional method to describe the hydrodynamic conditions is to plot the tube upstream pressure (p_u) against throat velocity (v_{th}) as shown in Figure 3-10 (a). The throat velocity derived from flow rate is defined as:

$$v_{th} = \frac{4Q}{\pi d^2} \tag{3.2}$$

As the cavitation generated bubble causes blockage effect to the liquid flow, the cavitation inception can be identified at the point where p_u starts to increase at a higher rate as v_{th} increases.

A more generic way to present the data is to use dimensionless number. In fluid dynamics, the resistance in a fluid environment is quantified by using the drag coefficient (c_d) defined as:

$$c_d = \frac{F_d}{\frac{1}{2}\rho v^2 A} \tag{3.3}$$

where F_d is the drag force, v is the flow speed, A is the reference area, and ρ is the mass density of the fluid. In a solid/liquid mixture system, ρ is defined as:

$$\rho = \frac{100}{(\frac{c_w}{\rho_s} + \frac{100 - c_w}{\rho_l})} \tag{3.4}$$

where c_w is the concentration of solids by weight, ρ_s and ρ_l are densities of the solid and liquid respectively.

Inspired by the drag coefficient concept, the pressure change induced by a Venturi tube is characterized by the flow resistance, also called loss coefficient, (L_c) defined as:

$$L_c = \frac{p_u - p_d}{\frac{1}{2}\rho {v_{th}}^2} \tag{3.5}$$

The potential of a flow to cavitate is characterized by the cavitation number defined as

$$\sigma = \frac{p - p_v}{\frac{1}{2}\rho {v_{th}}^2} \tag{3.6}$$

where p is a reference pressure and p_v the vapor pressure. p_v is constant at 2333 Pa in this study. The pressure was measured upstream and downstream leading to two possible definitions of the cavitation number:

$$\sigma_d = \frac{p_d - p_v}{\frac{1}{2}\rho {v_{th}}^2} \quad \text{and} \quad \sigma_u = \frac{p_u - p_v}{\frac{1}{2}\rho {v_{th}}^2} = L_c + \sigma_d \tag{3.7, 3.8}$$

Figure 3-10 (b) shows the plot of L_c in terms of σ_d that were converted from p_u and v_{th} in Figure 3-10 (a). As shown in equation (3.7), σ_d is inversely proportional to the square power of v_{th}, thus the increase in σ_d represents the decrease in v_{th}. In the no cavitation region at right of the Figure 3-10 (b), the loss coefficient is induced by only tube geometry and is linearly proportional to throat velocity. The loss coefficient at this regime is kept constant and denoted as L_{co}. Once the cavitation inception is reached, the extra loss coefficient, ΔL_c, induced by cavitation starts to arise as σ_d further decreases. By comparing these two plots, figure (b) delivered a global description of cavitation behavior with clearer indication of inception where L_c curve suddenly bends. Moreover, the constant value of L_{co} before cavitation inception can be used to quantify the system loss, which provide an easier solution for resistance comparison.

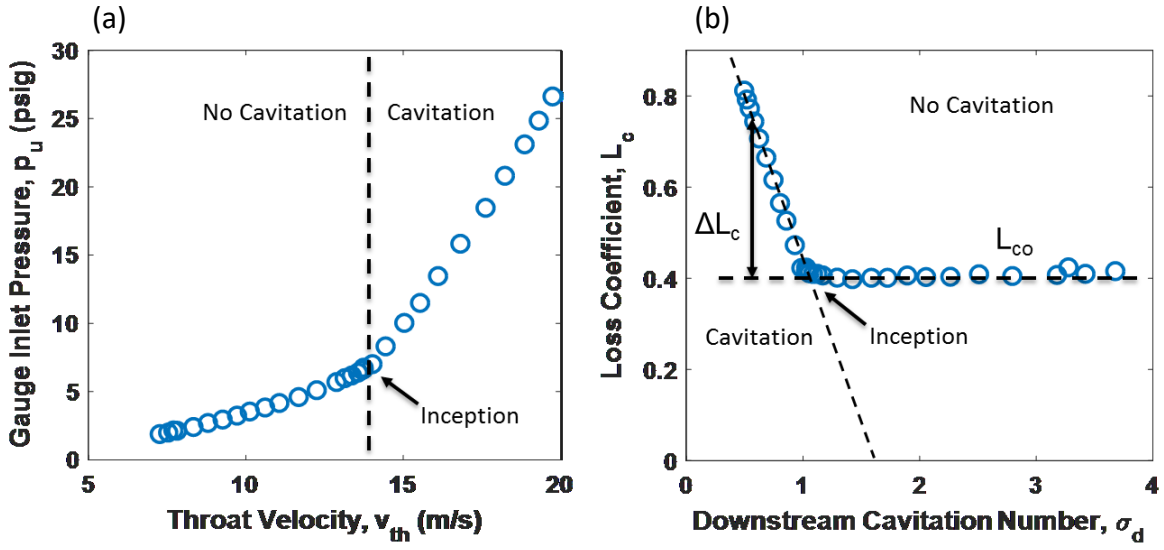

Figure 3-10. The hydrodynamic condition presented in (a) inlet pressure vs. throat velocity, and (b) loss coefficient vs. downstream cavitation number. This sample data was acquired by using a Venturi tube with geometry: outlet angle = 5° and diameter ratio = 4.

For the acoustic inception measurement in particle and bubble injection study, one seconds of 250k acoustic samples were measured for each loop. The inception is defined as the velocity

when 50% of the 250K samples have at least 4e-3 V amplitude in the raw acoustic wave. The fractions of cavitation samples (f) are named as cavitation probability. As the sample plot shown in Figure 3-11, the cavitation probability data displays a reversed cumulative distribution, and can be fitted by using the cumulative distribution function defined as:

$$f = \frac{1}{2}\{1 + \mathrm{erf}\left[\frac{-(\sigma_d - \mu)}{s\sqrt{2}}\right]\} \tag{3.9}$$

Where erf is the error function. By fitting the cavitation probability and the associated cavitation number data into function (3.9), the mean (μ) and standard deviation (s) of the distribution can be obtained. μ is regarded as the inception value because it represents the cavitation number when 50% of samples are cavitated.

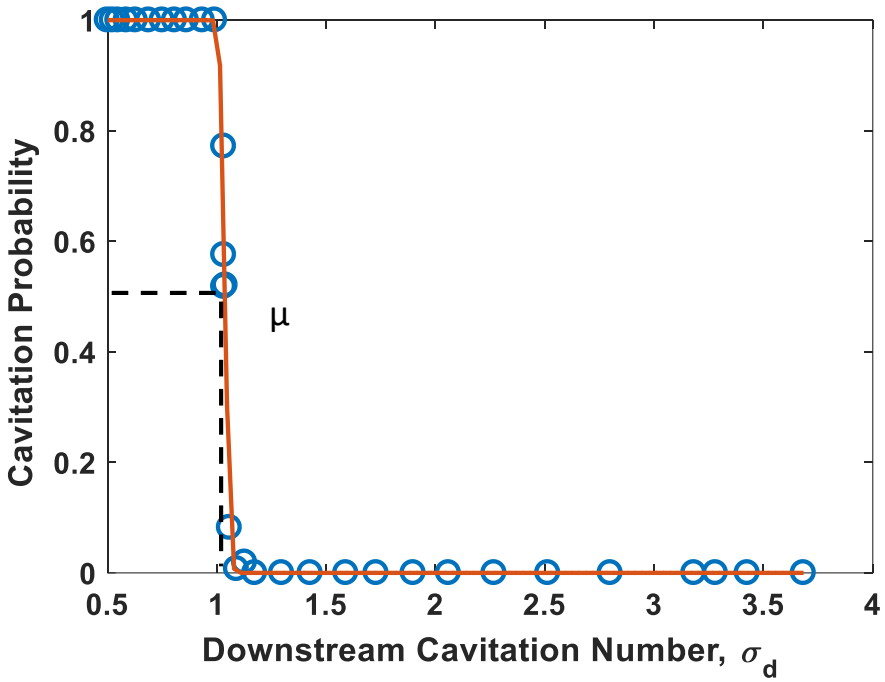

Figure 3-11. Example of cavitation probability in terms of downstream cavitation number with the indication of inception (μ).

3.5 Particle preparation and characterization methods

To prepare the fine particles for the 3-phase cavitation study, the crystalline bulk silica and graphite flakes were ground using the shatter box. As the grinding time increases from 1 min to 9 min, the particle sizes decreases, with a less and less rapid rate (Sanchez-Soto et al 1997). Spherical glass beads purchased from Kisker Biotech GmbH & Co. KG and graphite particles purchased from Sigma-Aldrich were also tested in the particle property study.

3.5.1 Mastersizer measurement

The Mastersizer 3000 laser diffraction particle size analyzer was used to determine the size and counts number of micron size particles. With the technology of laser diffraction, Mastersizer 3000 can deliver quick and accurate particle size distributions with a wide particle size range (Malvern 2013).

In the laser diffraction measurement, laser beams pass through the dispersed particles. Large particles scatter the light at small angles relative to the laser beam, while the small particles scatter light at large angles as shown in Figure 3-12. The angular variation in intensity of the scattered light is measured and analyzed to give the size of the particles. Having the combination of powerful blue and red light source, sensitive focal plane detector, and advanced optics, Mastersizer 3000 is able to measure the particle size range from 0.1 μm to 1000 μm. The particle size is presented as a volume equivalent sphere diameter (Slowik et al. 2004).

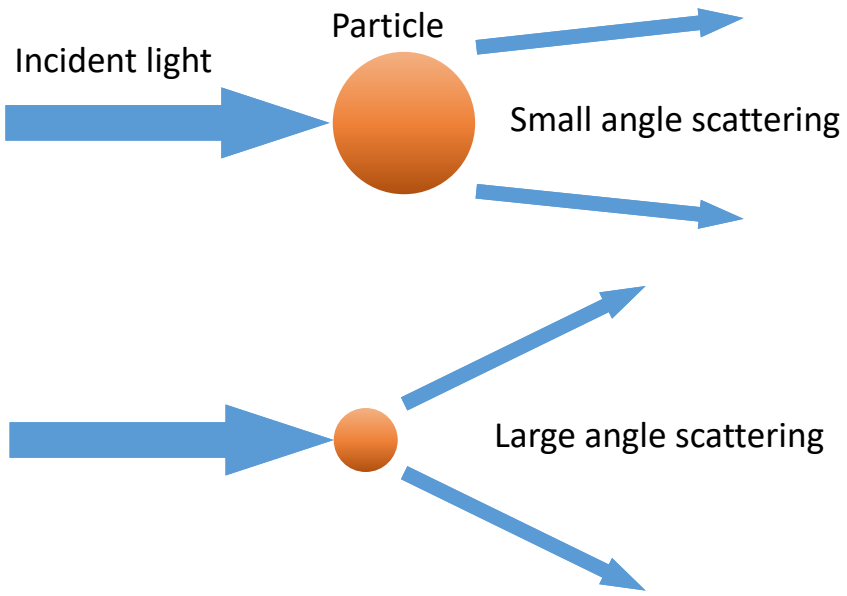

Figure 3-12. The angle of scattered light after light beam passes through particles with different sizes.

Table 3-2. Particle sizes with different grinding time measured using Mastersizer 3000.

Particle Name	Grinding Time (min)	D10 (µm)	D50 (µm)	D90 (µm)
Graphite	0.67	56.5	202	492
	1	28.3	120	321
	1.5	19.3	66.5	198
	2	19.9	66.2	199
Silica	5	3.62	23.8	105
	6	1.16	14.4	67
	7	0.917	11.5	53.6
	8	0.857	11.2	57.1
	9	0.799	9.91	46.6
Glass Bead	N/A	26.8	44	70.7

Table 3-2 lists the Mastersizer measured particle size distributions after different periods of grinding. D10, D50 and D90 represent the cumulative percentage point of the volume equivalent diameter. As shown in the table, the mechanical size reduction for graphite particles quickly becomes less effective after 1.5 minutes of grinding. On the other hand, silica particles still have a recognizable deduction in sizes after 9 minutes of grinding, resulting in the particles sizes way less than the minimum size of graphite.

3.5.2 Scanning electron microscope (SEM) imaging

Scanning electron microscope (SEM) was used to observe the surface patterns of particles in the cavitation study. To observe their surface structure, a microscope is required to provide high magnification and resolution of the images. Comparing to the conventional optical microscope, , SEM is able to provide a higher magnification with better resolution (Parry, 2000; Sytton et al., 2007). As the name suggests, SEM acquires image by shooting electron beams on the specimen. High-resolution images can be achieved by increasing the beam energy, thus decreasing the wavelength. The emitted electrons interact with the atomic structure of the specimen surface, and release radiation that is later on captured by the detector. The emitted radiation is composed of several components including secondary electrons (SE), back-scattered electrons (BSE), and other additional components. SE is the ejected electrons from the specimen after energized by the emitted electron, and it mainly used to obtain the topography of the specimen. On the other hand, BSE is the emitted electrons scatter by the specimen atoms; it can provide information about the atomic composition of the specimen. SE is mainly focused in this study because of the aim to have high-resolution topography without considering the composition of the specimens.

Figure 3-13 shows the SEM images of graphite, silica and glass beads. Graphite particles are flat with spongy edges. The soft structure has a good resistance to mechanical rupture, thereby explains the reason that size reduction by grinding is not as effective as silica.

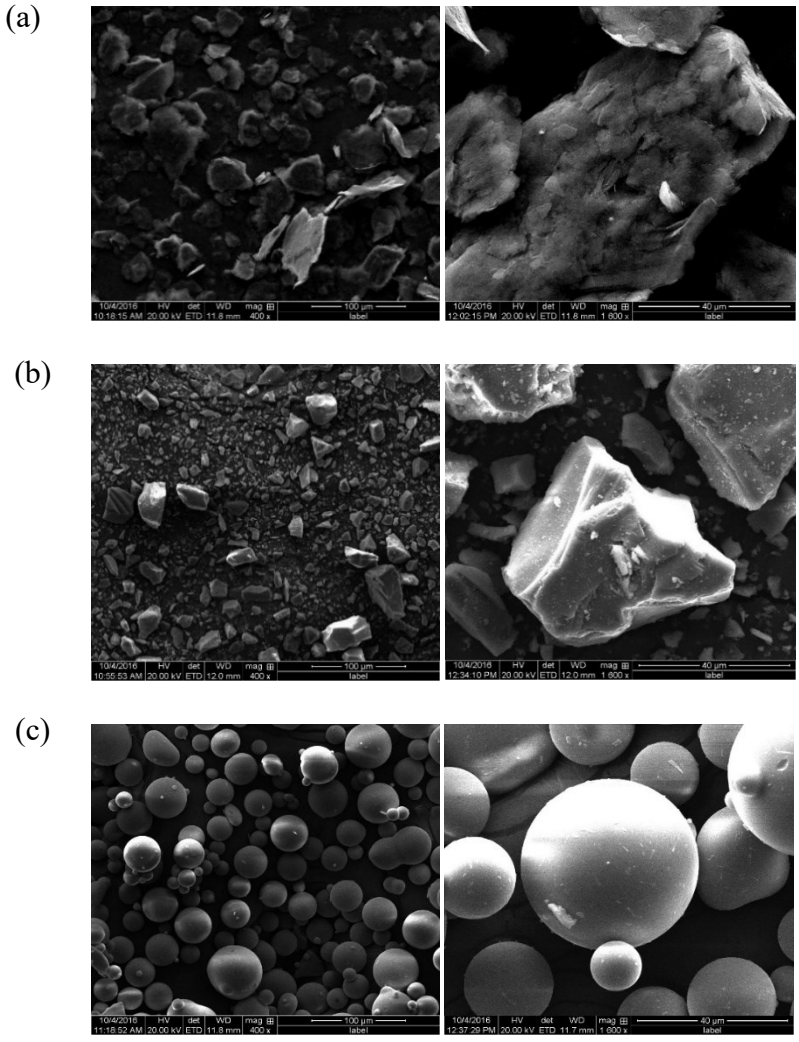

Figure 3-13. SEM images of particles at 400x and 600x: (a) graphite after 3 minutes of grinding, (b) silica after 5 minutes of grinding, and (c) glass beads.

3.5.3 Contact angle measurement and hydrophobic bath

The wettability of the particles is an important parameter especially in the study of effect of particle properties on cavitation. The contact angle that is formed by a liquid at the three-phase boundary has been used to quantitatively describe the wettability. In this study, the material contact angle was measured by using KRUSS optical Tensiometer (Biolin Scientific). To avoid the error induced by Wenzel or Cassie-Baxter effect, this measurement requires a flat material surface to be tested on. For the contact angle measurement of bare silica, A silica wafer with a flat surface was prepared by polishing the bulk material. The contact angle of the bare silica is around 8^{o}, indicating the bare silica hydrophilic surface property.

The process of hydrophobic bath was used to anchor the hydrophobic coating on the surface of silica particles. 1 mM of dimethyldichlorosilane (DMDCS) in toluene solution was prepared as the bath solution. Silica particles were immersed in the solution for 10s and recollected through filtration. As shown in Figure 3-14, during the treatment process, DMDCS peeled off the hydrophilic hydroxyl group from the silica surface, and substituted with a layer of methyl group that is repulsive to water molecules. Since it is difficult to measure the contact angle directly on silica particle, a piece of silica wafer was prepared and treated with DMDCS solution following the same procedures. By using Tensiometer, the contact angle of silica wafer was found to be around 65^{o}, indicating an apparent increase in particle hydrophobicity after the treatment.

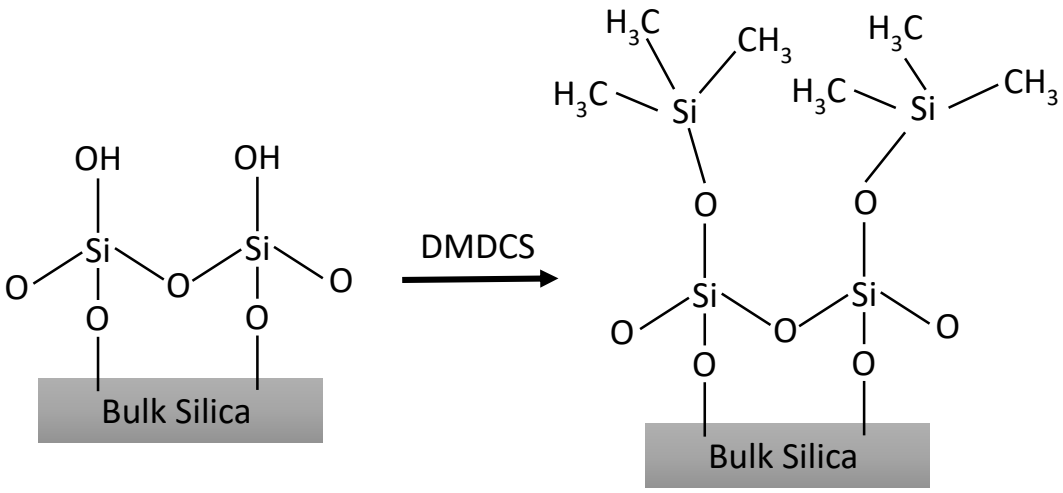

Figure 3-14. Schematic depiction of forming a hydrophobic coating with DMDCS on silica surface.

3.5.4 Film flotation

Although the conventional contact angle measurement has long been used to access the wetting behavior of solids, the angle measurement of a droplet on the packed silica particle yields questionable hydrophobicity (Bormashenko et al., 2007) because Cassie-Baxter or Wenzel effects are induced by the presence of gaps or crevices between the surface particles.

Film flotation is a technique that provides an alternative solution for assessing the wettability of particles (Fuerstenau and Williams, 1987; Liu and Xu, 1996). In this method, particles are placed on the surface of methanol-water solutions with various surface tensions. The transfer of particles from the vapor phase to the liquid phase involves four states schematically shown in Figure 3-15. Two groups of particles will be separated based on their behavior in the test. The particles are considered lyophobic if they do not go beyond state III where the liquid wets the particle and dissipates its kinetic energy from the state I to II. On the other hand, the

lyophilic particles are those in state IV where the particles are completely wetted and sink into the liquid. Whether the particles exhibit lyophobicity or lyophilicity theoretically depends on the wettability, size and density of the particle. However, Diao and Fuerstenau (1991) experimentally proved that the particle size, density, shape, and time have a negligible effect on the flotation results. Therefore, the particles wettability can be represented by the surface tension of the wetting liquid at which the particles are imbibed.

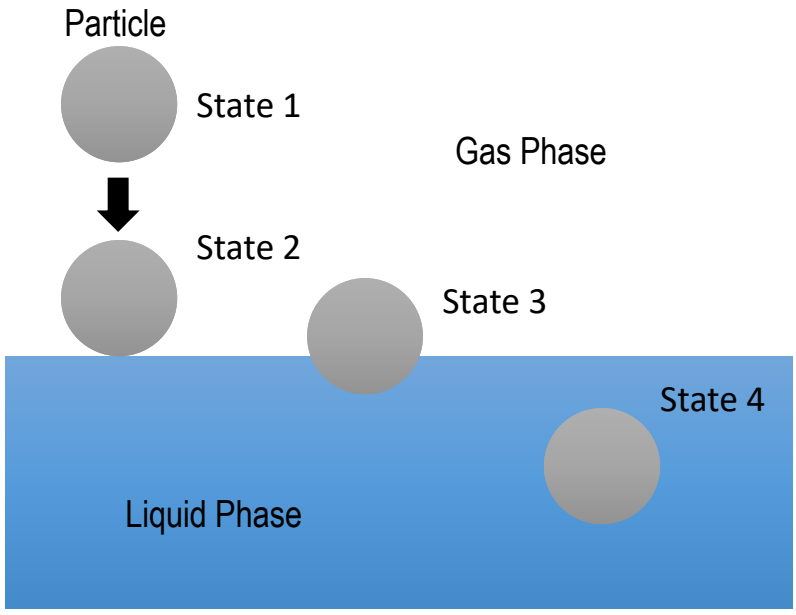

Figure 3-15. Schematic representation of the four states involves in film flotation. This figure is re-plotted according to Diao and Fuerstenau (1991).

The fractions of lyophobic particles regarding to the surface tension of methanol solutions are shown in Figure 3-16. γ_c^{min} and γ_c^{max} are the surface tensions of the solutions that wet all particles and no particle respectively. $\overline{\gamma_c}$ is the mean critical wetting surface tension. Zisman (1964) correlated the contact angle, θ with γ_c by

$$\cos\theta = 1 - b(\gamma_{LV} - \gamma_c) \tag{3.10}$$

where γ_{LV} is the liquid surface tension and b is a constant number ranged from 0.03 to 0.04. Based on the equation, the hydrophobicity of particle is negatively proportional to its critical wetting surface tension.

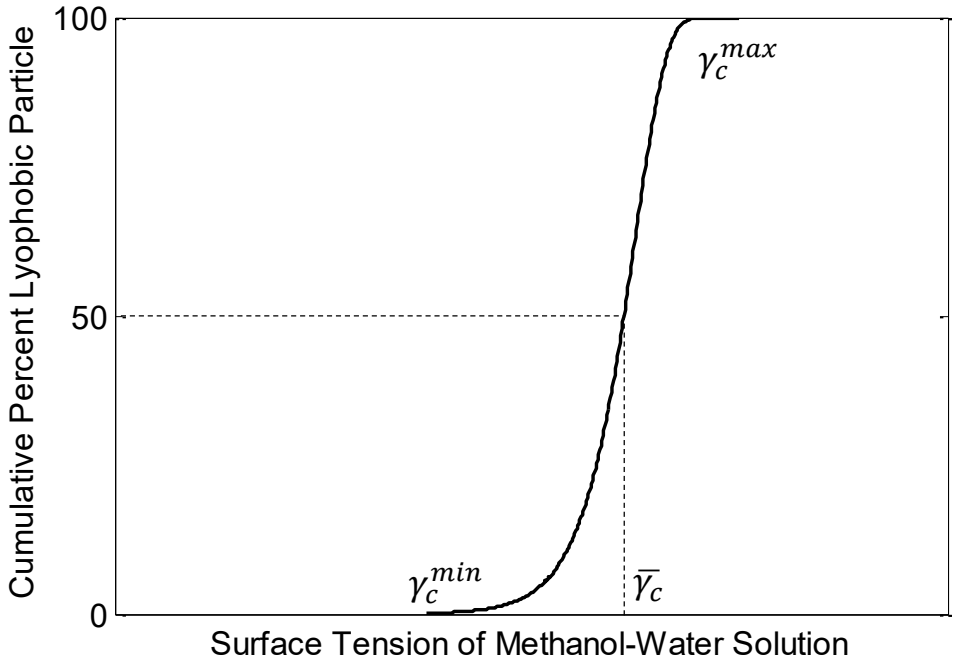

Figure 3-16. Cumulative percentage of particles not imbibed by the liquid and the indications of wetting surface tensions.

Chapter 4 Results and Discussion of Venturi Geometry Study

In the Venturi tube geometry study, I focused on four geometrical parameters: inlet angle, throat length, outlet angle, and diameter ratio. For a preliminary understanding of the effect of geometry, single-phase numerical simulations were performed in advance to help indicate the critical parameters that require further experimental investigation.

4.1 CFD simulation of Venturi tube pressure profile

The numerical simulation provides the pressure profile along different tube models at the same throat velocity of 20 m/s (Figure 4-1). Pressure evolution follows the same trend regardless the geometry: the pressure starting higher at the inlet decreases at the throat since the liquid is accelerating according to Bernoulli's principle. It then increases in the outlet to recover to the atmospheric pressure. The inlet pressure differs from the outlet pressure due to viscous loss, which depends on the tube geometry. To identify the critical geometric parameters on cavitation behavior, I focused the analysis on the inlet and throat pressures. The throat pressure is a good indicator of the cavitation as lower pressure represents higher tensile strength. Bubble nucleation is expected when the tensile strength reaches a critical value. In addition, the inlet pressure characterizes the loss and thus the power consumption of a tube. Although single-phase simulations cannot accurately predict inlet and throat pressures, it allows us to identify a global trend and determines the critical geometrical parameters.

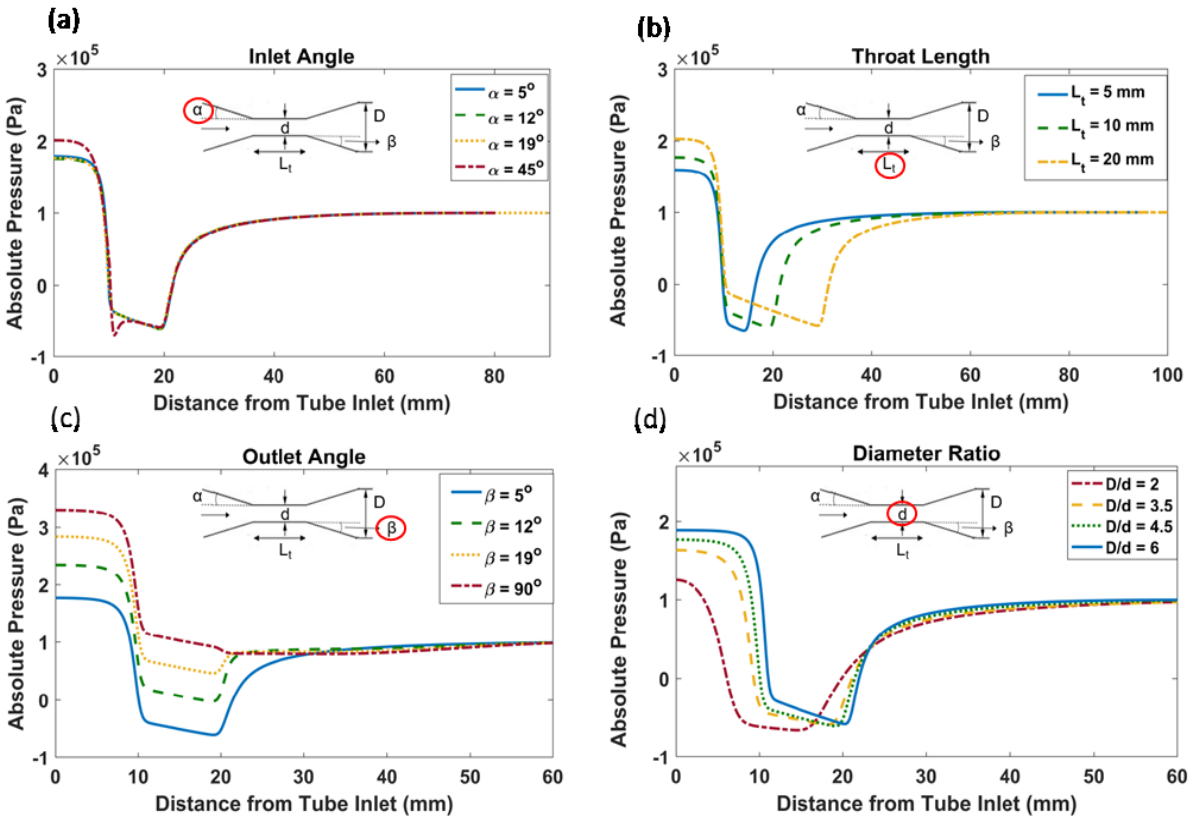

Figure 4-1. Pressure profile along the Venturi tubes at 20 m/s throat velocity with different geometrical parameters: (a) inlet angle, (b) throat length, (c) outlet angle, (d) diameter ratio.

Figure 4-1 shows the comparison of liquid pressure profile along the center of different Venturi tubes for a fixed throat velocity of 20 m/s. Figure 4-1a and b compare pressure profiles across different inlet angles (α) and throat lengths (L_t). Inlet and throat pressures are shown to be similar regardless of the geometry, indicating a limited effect of the two parameters on cavitation behaviors. Therefore, the inlet angle and throat length can be eliminated in further experimental studies. In contrast, Figure 4-1c shows the outlet angle (β) strongly affecting the pressure profile in the tubes. As the outlet angle increases both the inlet and throat pressures increase. This trend originates from eddy formation at the outlet due to the sudden expansion.

Figure 4-2 shows the comparison of streamlines for two tubes with different outlet angles. The higher the outlet angle, the larger the recirculation. This results in an extra loss and higher inlet pressure which in turn increase the throat pressure. For different diameter ratios (Figure 4- 1d), similar inlet and throat pressures are observed. However, the same throat velocity requires differing flow rates resulting in different power consumptions. Based on these preliminary simulations I identify two key geometric parameters: the outlet angle as it strongly affects the pressure profile and the diameter ratio for its influence on the power consumption.

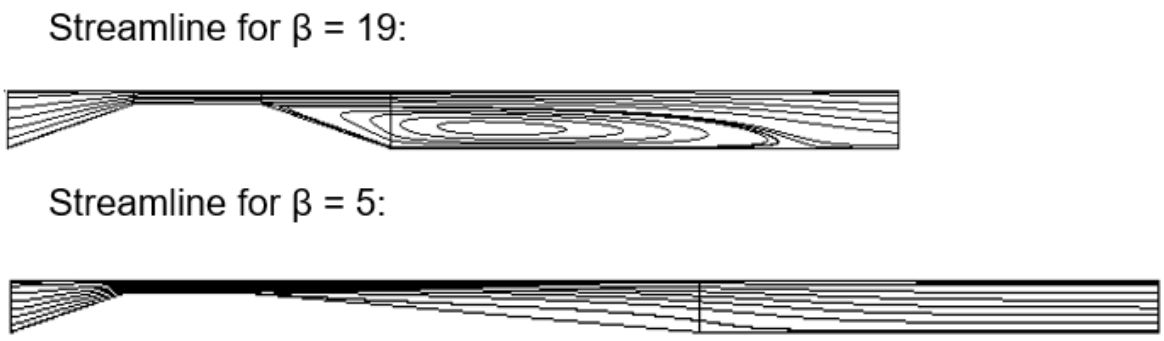

Figure 4-2. The CFD single-phase simulation generated streamlines for two tubes with outlet angle of 19^{o} and 5^{o}.

4.2 Effect of Venturi geometry on cavitation inception

Having identified the critical geometrical parameters above, their effects on power consumption and cavitation behavior were experimentally investigated by testing six fabricated Venturi tubes with different outlet angles and diameter ratios. Their 3D models are shown in Figure 3-3.

To investigate the power consumption and demonstrate the observation of inception studied above, the inception throat velocity (v_{th}^{in}) and the inception power (P^{in}) of different outlet angles are compared as shown in Figure 4-3. v_{th}^{in} and P^{in} were calculated using equation (3.2) and (3.1) respectively and the inception is indicated by using the acoustic method. An increase of the inception velocity with the outlet angle was observed as shown in Figure 4-3 a. This trend was anticipated in the simulation part as the pressure in the throat increased with the outlet angle due to the extra loss induced by large eddied at the outlet. To reach the cavitation inception, a higher velocity is required to overcome the pressure lost. Consequently, the inception power drastically increases (by a factor of 5 from 5° to 90°) due to high pressure loss and high velocity.

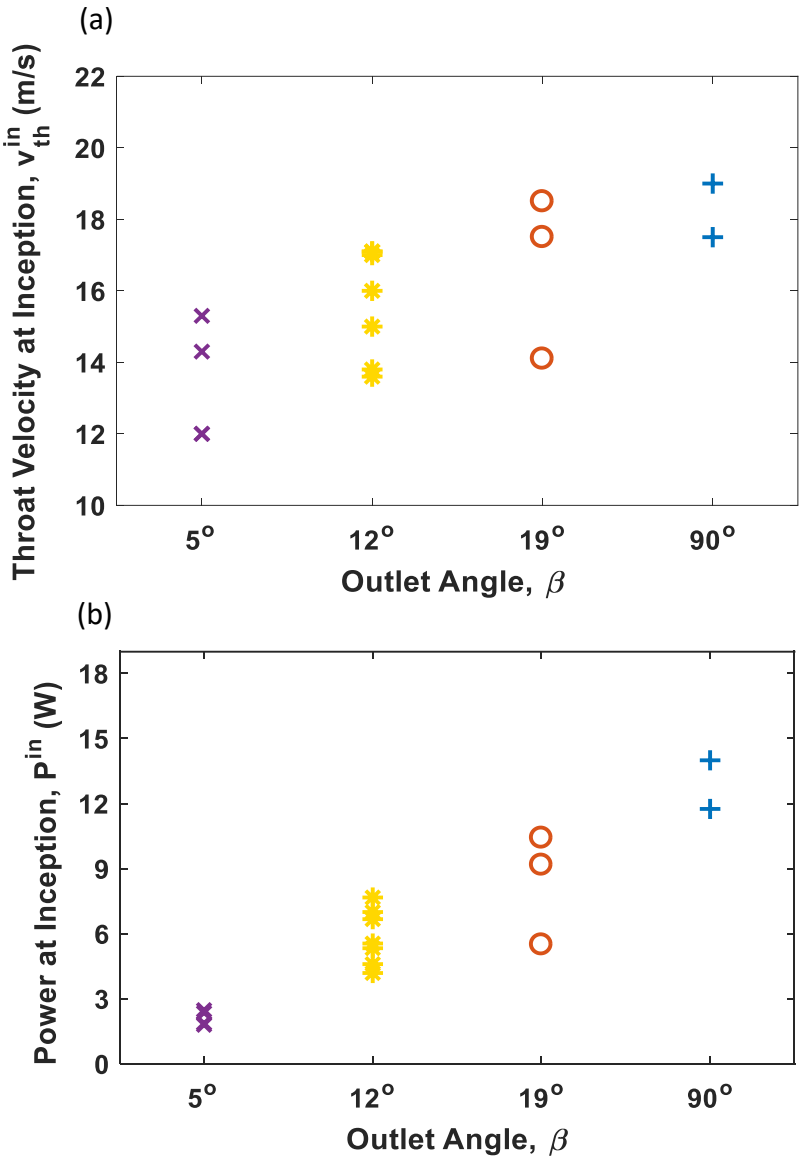

Figure 4-3. (a) Throat velocity and (b) power at cavitation inception for different outlet angles.

For the diameter ratio comparison, the throat velocity at inception is constant (Figure 4-4). The correlation has a good agreement with the simulation results where similar throat pressures were found at the same throat velocity regardless of the diameter ratio. The inlet pressures were

also shown to be similar in simulation, however, the inception power increases with decreasing diameter ratio. This is due to the higher flow rates requirement for the low ratio to achieve similar throat velocities, resulting in a higher power consumption to reach the inception pressure.

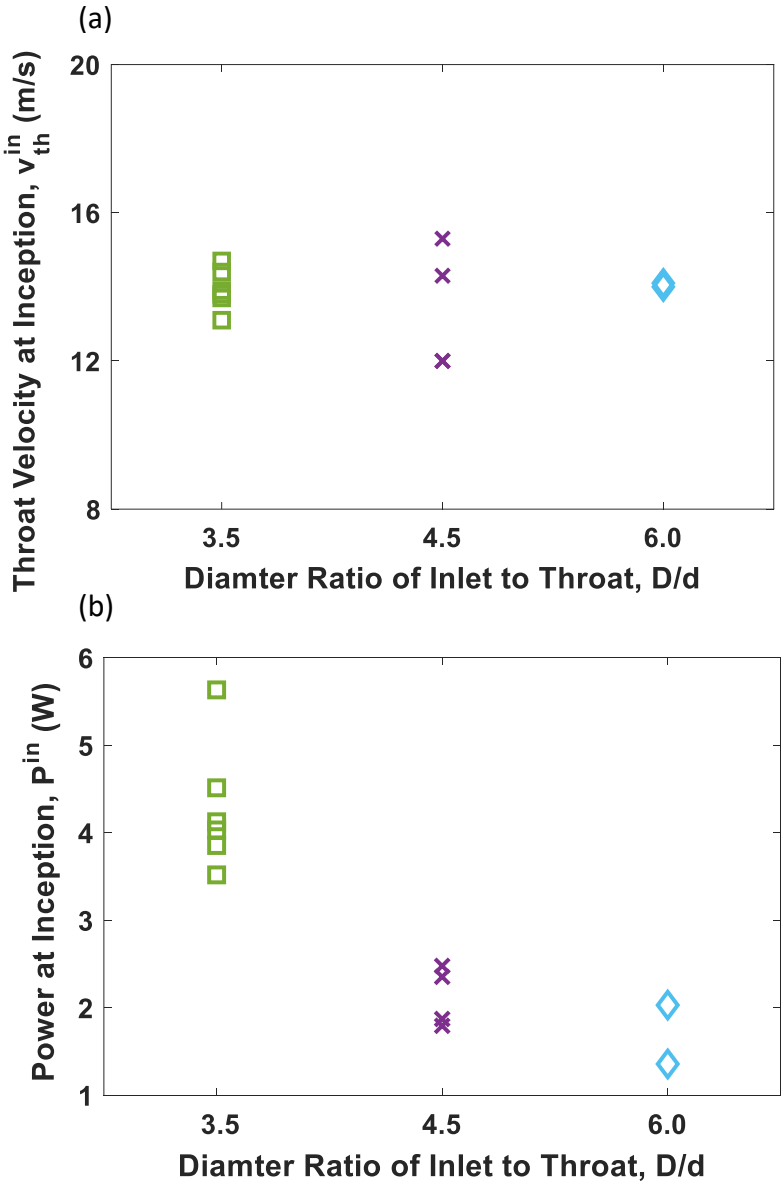

Figure 4-4. (a) Throat velocity and (b) power at cavitation inception for different diameter ratios.

4.3 Cavitation behavior expressed by loss coefficient

In the previous section, I studied the synergy between geometry and the cavitation inception and highlighted the influence of the pressure loss on the inception determination. To further explore the correlation between cavitation inception and geometry, the evolution of the loss coefficient (L_c) in terms of the cavitation number (σ_d) were compared for the different tubes in Figure 4-5. It should be noted that σ_d is inversely proportional to the square power of v_{th}, thus a high σ_d indicates a low flow velocity. As described in section 3.4, two regimes can be identified: a single-phase regime at high cavitation number (right of the dash line) where the loss coefficient is constant. In the second regime, flow is cavitating at low cavitation number where the loss coefficient linearly increases as the cavitation number decreases.

In the first regime, the loss coefficient exhibits a clear correlation with the outlet angle. As anticipated, the dissipation associated with large eddy formation increases the flow resistance of big outlet angle tubes. Alternatively, different diameter ratios show only a slight loss coefficient deviation indicating a similar flow structure at the same divergent angle. Once the cavitation starts, regardless of the geometry all the loss coefficients collapse into a single curve corresponding to a constant upstream cavitation number. Under cavitating flow, the throat pressure remains constant and is equal to the vapor pressure (Randall, 1952). Consequently, the inlet pressure only depends on the convergent geometry and the vapor pressure that results in a fixed upstream cavitation number. This result reveals that the pertinent cavitation number to describe the hydrodynamic cavitation is the upstream cavitation number (σ_u) as it takes into account the tube geometry through the inlet pressure. It is also interesting to note that the cavitation inception can be seen as the interception between the single-phase loss coefficient

(L_{c0}) and the constant inlet cavitation number (σ_u). Low flow resistance tubes (small L_{c0}) have a higher inception downstream cavitation number (σ_d^{in}) as shown in the inception study.

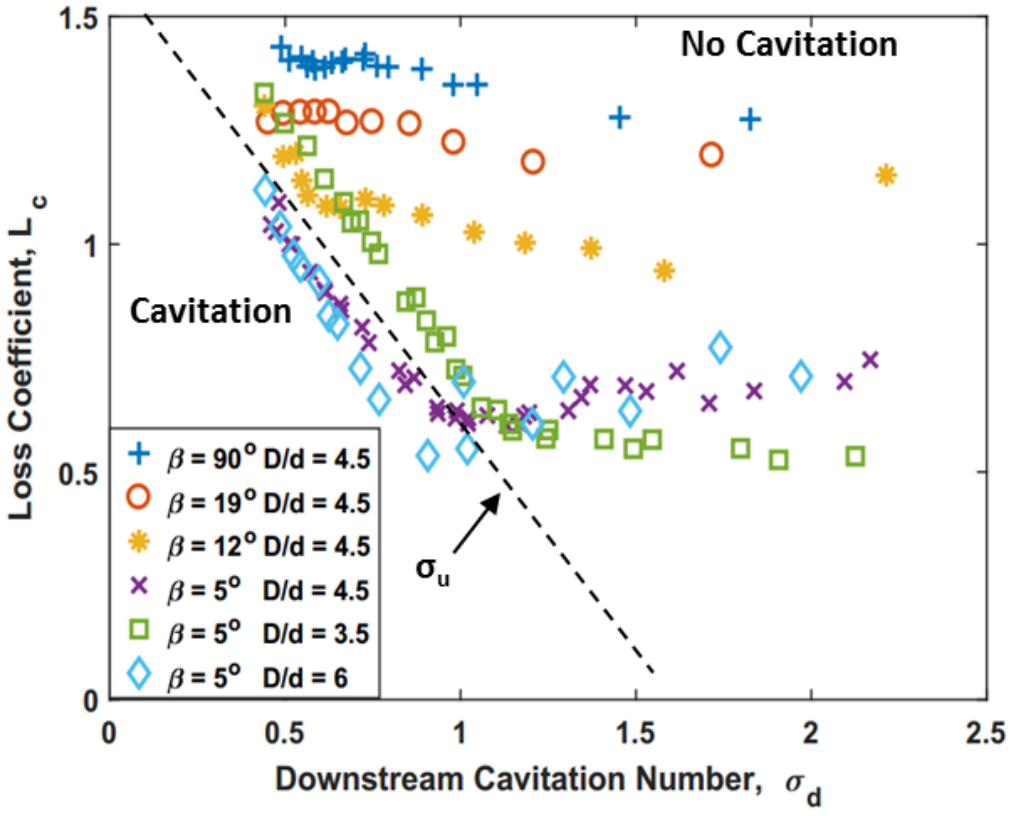

Figure 4-5. Loss coefficient in terms of downstream cavitation number for different Venturi tube geometries.

4.4 Effect of Venturi geometry on bubble generation

The cavitation phenomena consist of the nucleation of bubbles inside a liquid where the local pressure drops below the saturation pressure. As the pressure recovers, a part of this bubble collapses while the other part can be stabilized by the dissolved gas inside the liquid and therefore can be recorded with a high-speed camera. This nucleation process is associated with an increase of the loss as shown in Figure 4-5.

In Figure 4-6, the cumulative bubble volume recorded by the camera is plotted against the extra-loss induced by the cavitation defined as the difference between the loss coefficient under cavitation and the single-phase loss coefficient (L_{c0}):

$$\Delta L_c = (L_c - L_{co}) \tag{3.5}$$

Table 4-1. The average single-phase loss coefficient L_{c0} for the different geometries.

Tube Design	Mean System Loss, L_{co}	Standard Deviation
β=90° D/d=4.5	1.372	0.047
β=19° D/d=4.5	1.250	0.042
β=12° D/d=4.5	1.030	0.072
β=5° D/d=4.5	0.621	0.013
β=5° D/d=3.5	0.583	0.032
β=5° D/d=6	0.669	0.075

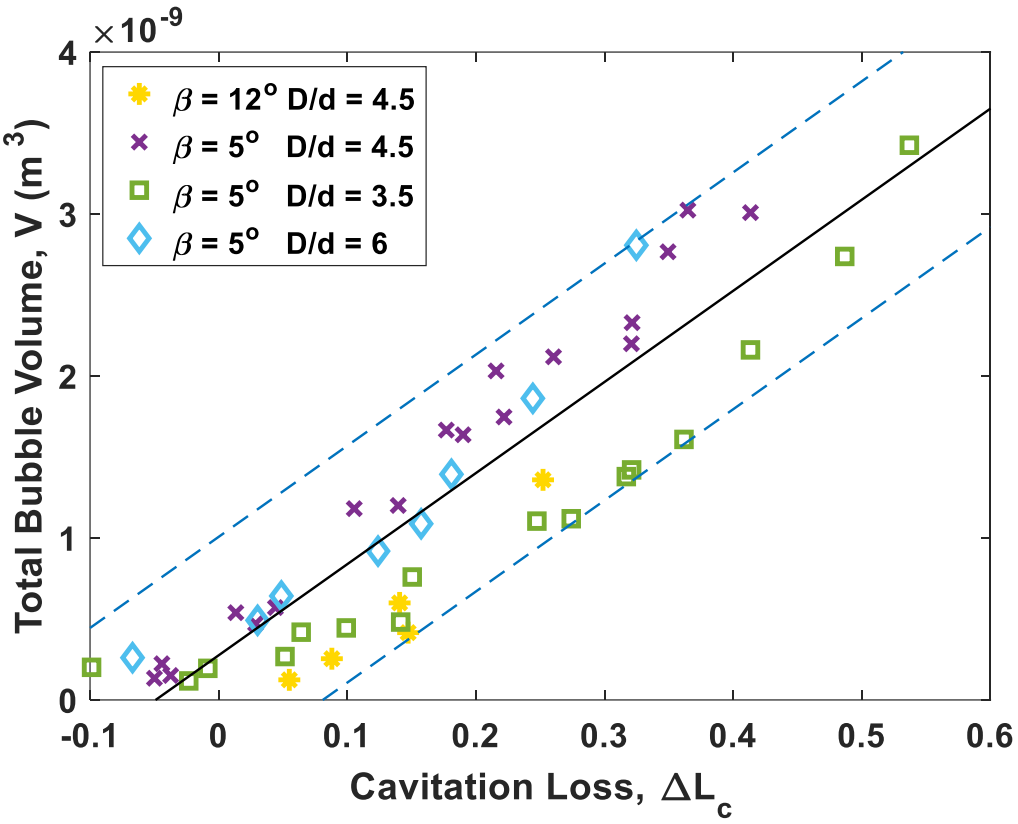

Figure 4-6. Total bubble volume as the function of cavitation loss for different tube designs.

The average loss coefficients before cavitation were extracted from Figure 4-5 and are summarized in Table 4-1. It should be noted that for the outlet angle of 19° and 90° were excluded in the Figure 4-6 since no significant amount of bubbles was recorded. As shown in the figure, all the data follows the fitting line within +/- 7.31e-10 m^3 error range regardless of the geometry. The bubble volume increases linearly with the cavitation loss (ΔL_c), which means the bubble generation depends on the extra energy added to the system once the cavitation starts. Therefore, the tube efficiency regarding the cavitation process is determined by the inception point; the earlier the inception, the larger the amount of bubbles generated. In conclusion, the tube geometry fixes the single-phase loss coefficient (L_{co}) which in turn controls the cavitation inception and activity (bubble generation and collapsing).

4.5 Effect of dissolved air on bubble generation

As discussed in the previous section, the stabilization of nucleated bubbles is controlled by the transfer of the dissolved gas into nucleated bubbles. Previous experiments were carried at a fixed amount of dissolved gas by insulating the air from the liquid in the flow damper (air entrapped into balloons). The influence of the dissolved gas was investigated by removing the balloons allowing the air to dissolve into water inside the pressurized flow damper.

The total amount of bubbles with and without air insulation in terms of cavitation loss is shown in Figure 4-7. The total amount of bubbles increases faster without balloons (Figure 4-7 a) indicating that more bubbles are stabilized. The dissolved gas concentration is governed by Henry's Law (Sander, 2015) and is proportional to the air pressure in the gas phase. As shown in Figure 4-7 b, the normalization of the total bubble volume by the atmospheric pressure in the insulated case and by the upstream pressure (pressure in the flow damper) in the other case collapses all data into a single line. This linear correlation between bubble volume and air pressure reveals that the bubble generation and stabilization are proportional to the dissolved gas concentration.

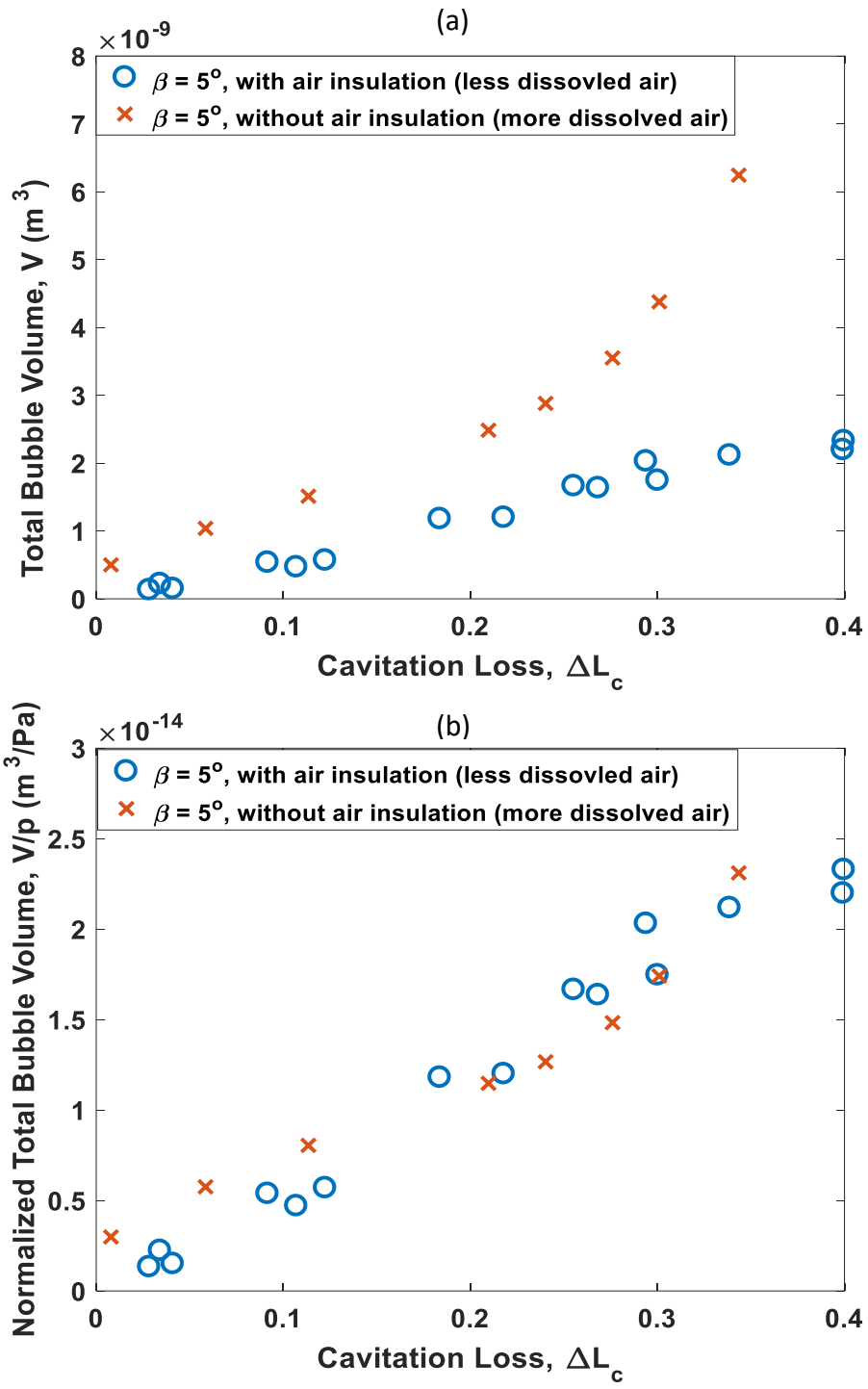

Figure 4-7. (a) Total bubble volume and (b) normalized bubble volume in terms of the cavitation loss with and without water-air insulation for a diameter ratio of 4.5 and outlet angle of 5°.

Chapter 5 Results and Discussion of particle and bubble influence on hydrodynamic cavitation behavior

The bubble generation in cavitation processes is regarded as heterogeneous nucleation because of the presence of solid and gas content in liquid phase providing sites with lower energy barrier for bubble generation. Correspondingly, hydrodynamic cavitation can be theoretically promoted by the presences of the solid/liquid interface, crevice structure of the solid surface, and the pre-existing bubbles. In the Venturi tube geometry study of last Chapter, hydrodynamic cavitation experiments were performed with merely tap water. The bubble nucleation took places on sites including the tube wall and suspending gas nuclei, but the number and strength of the sites were hard to manage. Modern industrial applications such as mineral flotation involve hydrodynamic cavitation associated with particles slurries and bubble injection. To better investigate the practical cavitation behavior involving particles and bubbles in the fluid, a multi-phase system is required in the experimental study. In this Chapter, particles with different wettability, concentration, surface structures, and bubbles with different injection rates were introduced into the liquid system to investigate the effect of particle and bubble addition on hydrodynamic cavitation.

5.1 Particle characterization

Table 5-1. Properties of tested particles

Particle Name	Contact Angle (°)	Structure	D50 (μm)
Graphite	N/A	Irregular Flake	66.2
Bare Silica (BS)	8	Irregular	23.8
Treated Silica (TS)	65	Irregular	23.8
Glass Bead (GB)	N/A	Smooth spherical	44

Bare silica (fresh silica after 5 minutes of grinding), treated silica (bare silica with hydrophobic treatment), graphite (graphite flakes after 2 minutes of grinding), and glass bead are the four types of particles that were tested in the particle effect study. Their properties obtained from section 3.5 are listed in Table 5-1. In Figure 3-13, the SEM images of particles are shown. The glass beads exhibit spherical shape with a relatively smooth surface. On the other hand, silica and graphite particles have irregular shapes with crevices distributed on the surfaces. The Mastersizer measurement of particles sizes shows the graphite to have the largest mean diameter because the soft edges on the graphite flakes weakened the effect of grinding. Followed by the glass beads, silica particles are the smallest among all. The treated and untreated silica particles have approximate contact angles of 8° and 65° respectively. The angle measurements were performed on prepared flat surfaces made of the same material. Realizing the difficulties in measuring the contact angle of graphite and glass bead, the method of film flotation was adopted so the particles' wettabilities could be compared by looking at the critical

wetting surface tension. The high hydrophobicity can be indicated by the low critical wetting surface tension as discussed in section 3.5.4. In Figure 5-1, both bare silica and glass beads have almost zero fraction of lyophobic particles in the tested surface tension range, which indicate their wettability to be hydrophilic. The graphite shows a slightly lower critical wetting surface tension comparing to the last two, but the value is still much higher comparing to that of treated silica. Therefore, the treated silica substantially outperformed other particles in the hydrophobicity test.

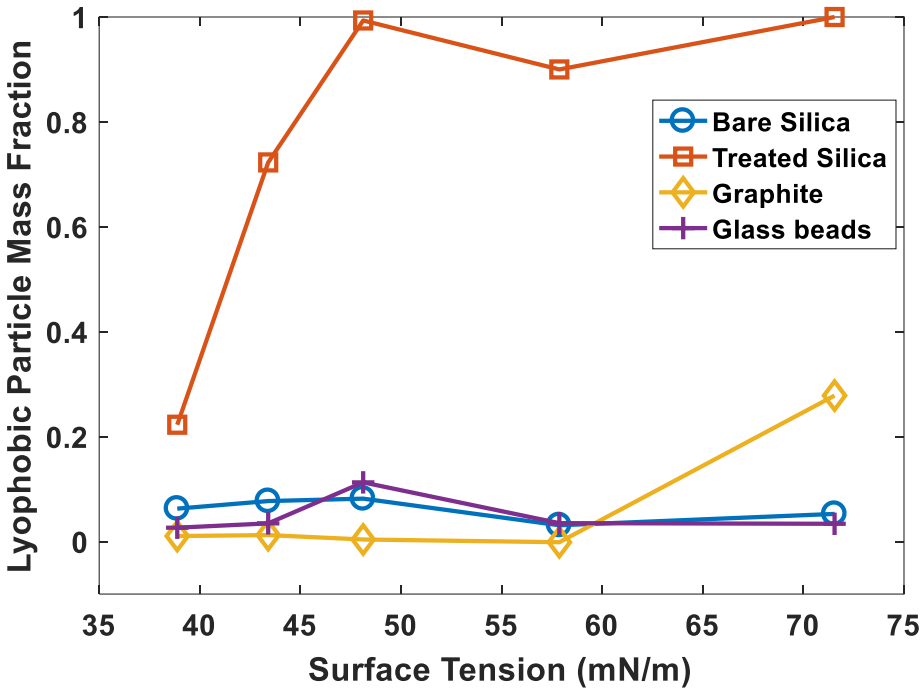

Figure 5-1. Lyophobic fraction of treated and untreated silica, graphite particles and glass beads in water-methanol solutions.

5.2 Effect of particle concentration on cavitation behaviors

To investigate the particle's concentration effect, bare silica particles after 5 minutes of grinding time were mixed with water at concentrations of 5 g/L, 10 g/L, 20 g/L and 150g/L. Slurries were pumped through the Venturi tube with geometry of D/d=4 and β=5° at flow rates from 4 LPM to 10 LPM. The experiments were performed both forwardly and backwardly. In the forward tests, flow was started at low rate and gradually increased, while the backward tests were conducted in the opposite way. Typically, at least 3 repeat measurements were made at each condition. The system flow rate and tube inlet pressure were measured simultaneously, and the recorded data are presented in the form of dimensionless number as shown in Figure 5-2 (a). Fitting lines derived by using "locally weighted scatter plot smooth" function in MATLAB were also plotted to display clear trends for particle concentration comparison. As explained in previous Chapters, the loss coefficient, L_{c0} in the no cavitation regime represents the loss induced by the resistance of Venturi tube on water flow. Figure 5-2 (a) shows that compared to the water run, the addition of bare silica particle increases the system loss, and the loss is further enlarged as the particle concentration increases. It could be due to the presence of particles hamper water from flowing through the setup, resulting in higher pump power and system pressure required for flowing water (higher viscosity). By comparing Figure 5-2 (a) with Figure 4-5, the system loss was lowered about 0.1. The discrepancy is due to the adjustment in the instrumental arrangement. The mixing tank was brought to the same height as the Venturi tube to eliminate pressure induced by to height difference, and the location of the flow meter was switched from downstream to upstream of the pressure transducer to avoid the resistance induced by the flow meter. Furthermore, a smaller flow damper was used to replace the big

cylindrical tank in order to minimize the amount of air dissolving in water at the pressurized condition.

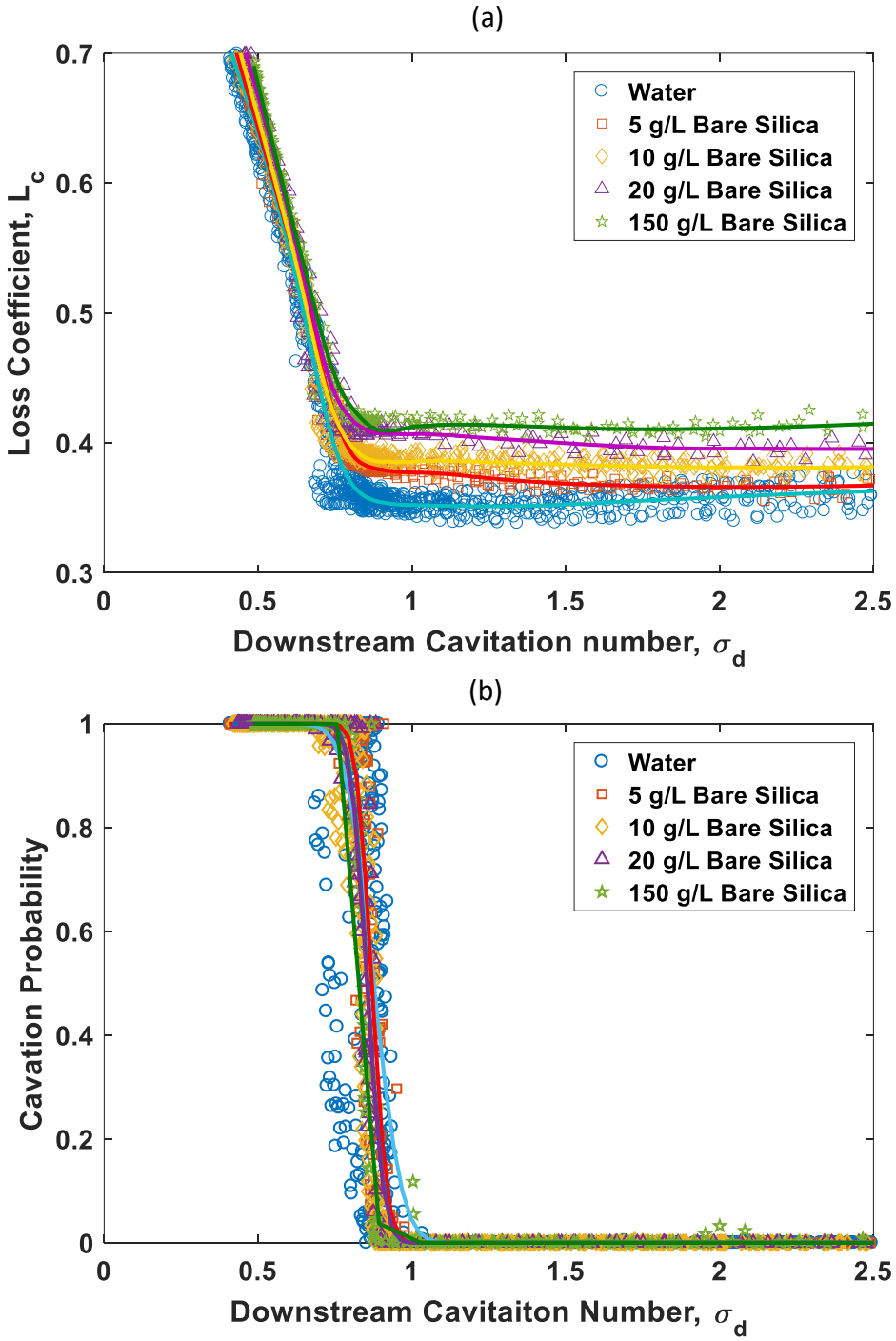

Figure 5-2. (a) Loss coefficient and (b) cavitation probability in terms of downstream cavitation number with bare silica slurries at different concentrations.

The acoustic power released from bubble burst was measured to indicate the cavitation inception. Derived from the acoustic data, cavitation probabilities of fluid with different bare silica concentrations are presented in Figure 5-2 (b). Their associated fitting lines were derived using equation (3.9). By examining the two figures, the point where L_c starts to arise from the constant value agrees with the expectation of the acoustic distribution in Figure 5-2 (b), indicating a good accuracy in inception measurement obtained by both loss coefficient and microphone. It is interesting to note that although the presence of bare silica increases the overall loss, no change the cavitation inception is observed in the concentration range from 5 g/L to 150 g/L. In the theory of conventional heterogeneous nucleation, the hydrophobicity of a flat solid surface can significantly affect the tensile strength required for bubble nucleation. According to the contact angle measurement, the bare silica is hydrophilic with the angle of ~ 8^o. It cannot provide sufficient reduction in the tension strength for bubble formation, thereby causing very less impact on the cavitation inception comparing to the water case. The results suggest that the population of hydrophilic particles does not affect the cavitation activities, but more energy needs to be consumed for the system with higher particle concentration to reach the inception velocity.

Although water and bare silica have similar inception as shown in Figure 5-2 (b), the data distribution exhibits a more scattered pattern without the addition of particles. To investigate this phenomenon, cavitation probability for forward and backward water testes are plotted separately in Figure 5-3. By increasing flow rate, the forward inception were measured to indicate the velocity when cavitation started, while the backward test recorded the velocity when cavitation ceased. Two observations can be obtained from the figure: the forward data shows a more scattered pattern, while the backward tests have more consistent inceptions with

generally higher values in terms of cavitation number (lower inception velocity). This hysteresis effect could be due to the existence of gas cavities produced by cavitation. As backward tests started in an already cavitating system, the pre-existing cavities provided gas nucleation sites with low tensile strength requirement for bubble generation, thereby promoting cavitation to continue at velocity lower than the forward inception. On the other hand, the insufficient amount of cavities caused the forward water tests not able to cavitate as quick as the backward tests. By comparing Figure 5-3 with Figure 5-2 (b), the runs with particle addition exhibit similar cavitation behavior as the water backward tests since they all converge closely to the fitting line. It indicates that even though the bare silica does not affect the cavitation inception, it can provide adequate nucleation sites to ensure the cavitation to start as soon as the proper condition are met.

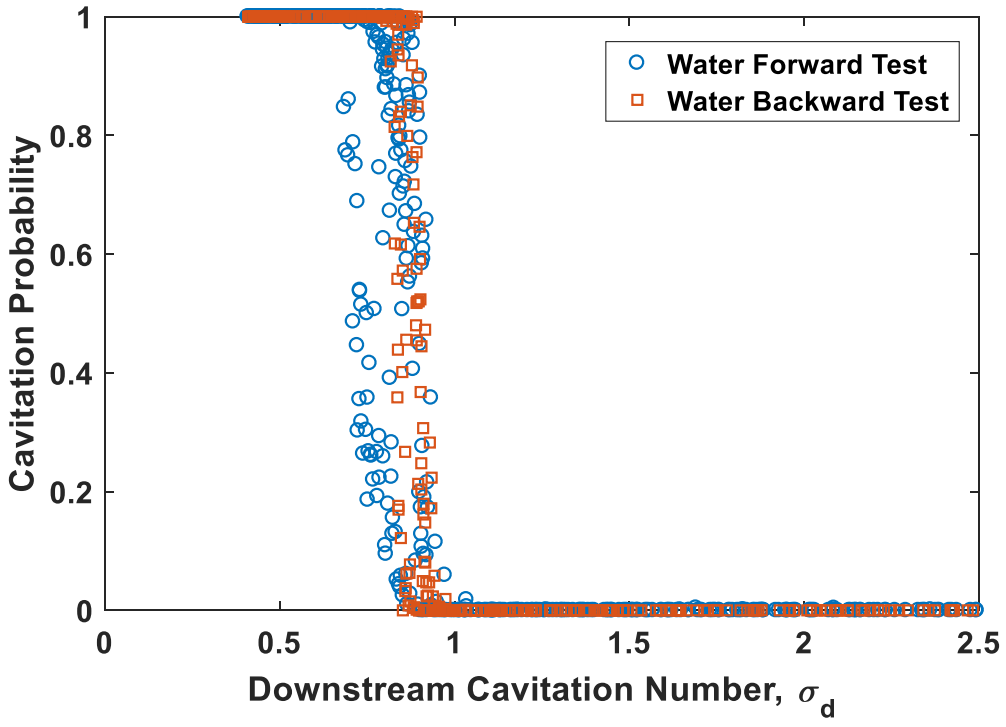

Figure 5-3. Cavitation probability for forward and backward water tests

5.3 Effect of particle wettability on cavitation behaviors

In the study of particle's wettability effect on cavitation behaviors, treated silica with contact angle ~65^{o} were mixed to the cavitating flow at the concentration of 5 g/L, 10 g/L, and 20 g/L. The hydrophobic-treated particles were prepared by immersing bare silica in the hydrophobic bath for 10 s.

The loss coefficient against cavitation number curves and the associated fitting lines are plotted in Figure 5-4 (a). As discussed in the last section, it is not surprising to observe the increase in the system loss as the particle concentration increases. By examining the cavitation probability curves plotted in Figure 5-4 (b), the presence of treated silica shows an earlier inception as compared to the water case. Having the treated silica particles provided solid surfaces with a higher hydrophobicity, the tensile strength required for bubble generation is lowered, and cavitation inception becomes easier. Moreover, the hydrophobic surface property enhanced the cavities immersing from the crevices, which would further promote nucleation when little tensile strength is applied. As the particle concentration increases from 5 g/L to 20 g/L, no noticeable change in the cavitation behavior is observed.

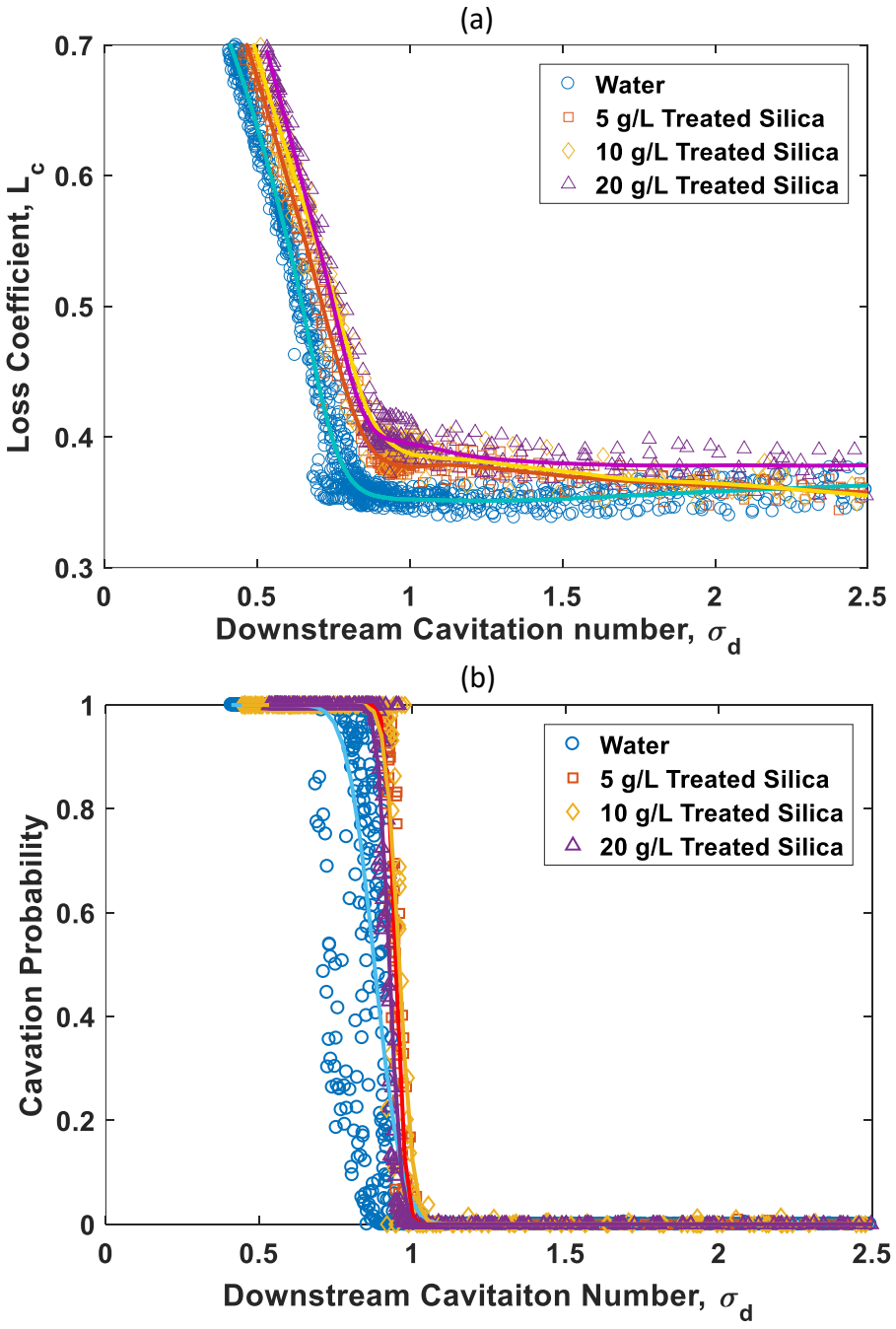

Figure 5-4. (a) Loss coefficient and (b) cavitation probability in terms of downstream cavitation number with hydrophobic treated silica slurries at different concentrations.

As described in section 3.5.4, the cavitation probability data can be fitted with an inversed cumulative distribution curve, and the value of cavitation inception can be quantified by the mean value of the distribution function. Figure 5-5 shows the both the forward and backward inception velocity with the addition of bare silica and treated silica at different concentrations. As anticipated, the inception of water forward tests exhibits a large variation because of the lack of nucleation sites. For most of the cases, backward inception velocities are lower than the forward ones due to the hysteresis effect. By looking at both the forward and backward inception, bare silica slurry and water exhibit the similar inceptions, which are about 7% higher than that with the addition of treated silica in the concentration range from 5 g/L to 20 g/L. The results on hydrophobicity and concentration's effect further demonstrate the conclusion from the loss coefficient curve.

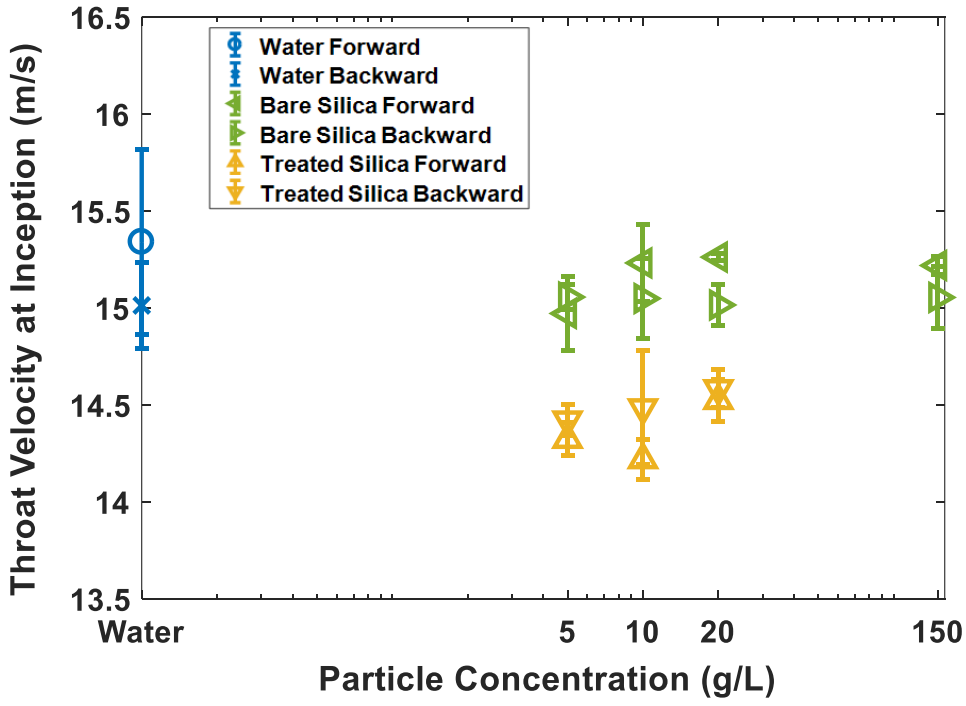

Figure 5-5. Throat velocity at inception in terms of particle concentration for silica particles with and without hydrophobic coating.

An interesting phenomenon was observed while conducting the reproducibility tests with treated silica. For the same batch of treated silica slurry, the repeated experiments exhibit slightly shifted inception comparing to the last run. To investigate this phenomenon, the hydrophobic particles after different periods of cavitation time were tested. The results plotted in Figure 5-6 shows the cavitation probability curves gradually approaching to the water run. The extracted inception velocities showed a clear increase from 14.3 m/s to 14.8 m/s through the 40 mins of cavitation time.

The increase in inception velocity could be due to the loss of particle hydrophobicity. To demonstrate this theory, in Figure 5-7 the hydrophobicities of fresh treated silica and that after 1 hour of cavitation were compared using film flotation. Referring to the bare silica that has 0 fraction of lyophobic in the tested surface tension range, more than half of TS lost its hydrophobicity after 1 hour of cavitation since only ~0.4 fraction of TS particles could still maintain the original lyophobic behavior. In the hydrophobic treatment process, a layer of hydrophobic functional groups was chemically anchored on the silica particle surfaces. However, the coating is not permanent, and the particle would lose its hydrophobicity if the coating material is mechanically peeled off in a strong force field. As discussed in section 2.1, the collapse of bubbles in cavitation process is associated with high local pressure and temperature that is able to cause erosion by removing the material from the surface. Besides cavitation, the impeller in mixing tank operates at 1000 rpm rotating speed could also generate strong shear force that teared off the particle surface layers. Therefore, the longer the treated silica stays in the cavitating system, more hydrophobic functional groups would be destroyed, and its wettability becomes similar to the bare silica.

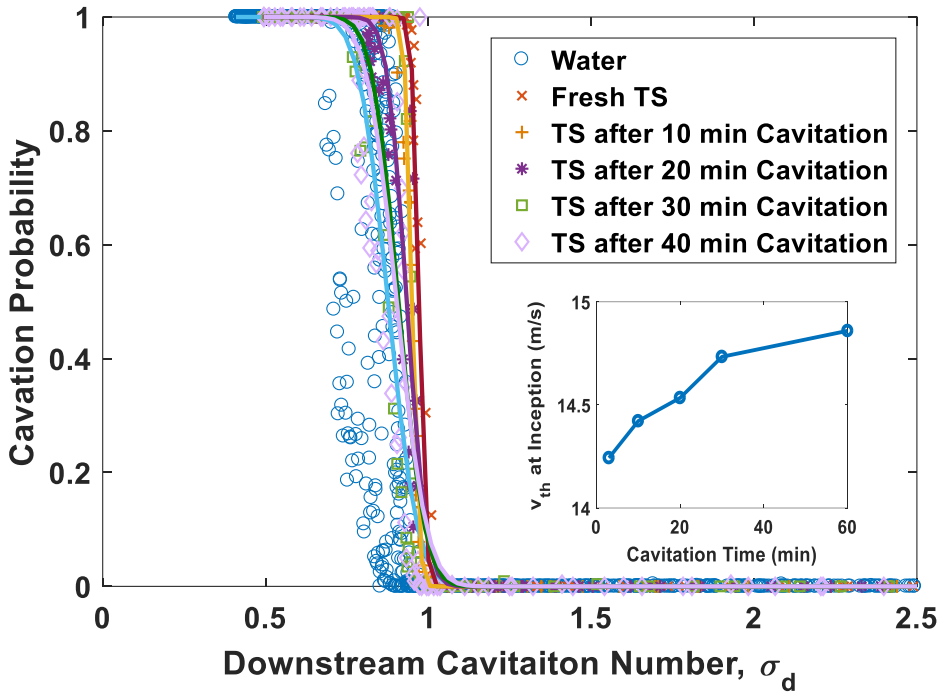

Figure 5-6. Cavitation Scale in terms of downstream cavitation number with 20 g/L treated silica slurry after different cavitating time.

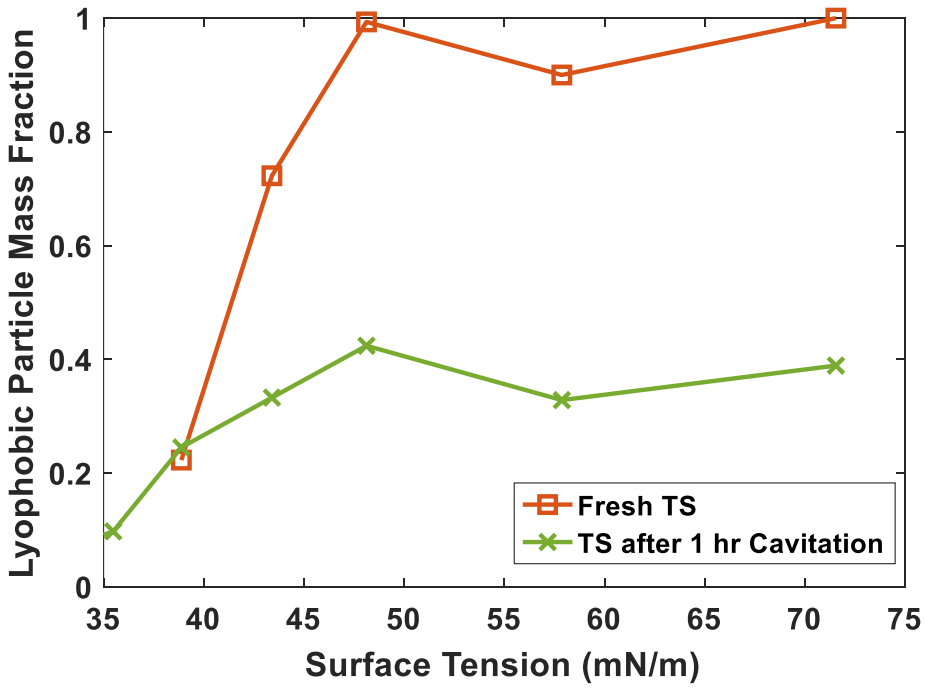

Figure 5-7. Film flotation of fresh treated silica particles and those after 1 hour of cavitation.

5.4. Effect of other particle addition on cavitation behavior

Glass beads and graphite particles were tested in the cavitation setup to acquire a general idea of other particles' effect on hydrodynamic cavitation. The loss coefficient in terms of downstream cavitation number for different particles and their associated inception velocity are shown in Figure 5-8. The particle comparisons were performed at the low concentration of 5 g/L because the infrared light emitted from flow meter could not penetrate through higher concentration of dark materials. Based on the thin film flotation test, glass beads are hydrophilic with similar wetting surface tension as the bare silica particles. In addition, their smooth spherical structural does not have crevices to facilitate cavities, thus the effect of glass beads on hydrodynamic cavitation is very limited. Although the graphite particles have slightly higher contact angle than bare silica and glass beads, they did not show any promotion on the cavitation inception neither. The acoustic measurement delivers similar results as the loss coefficient that the addition of graphite and glass beads does not have a noticeable on the cavitation behaviors.

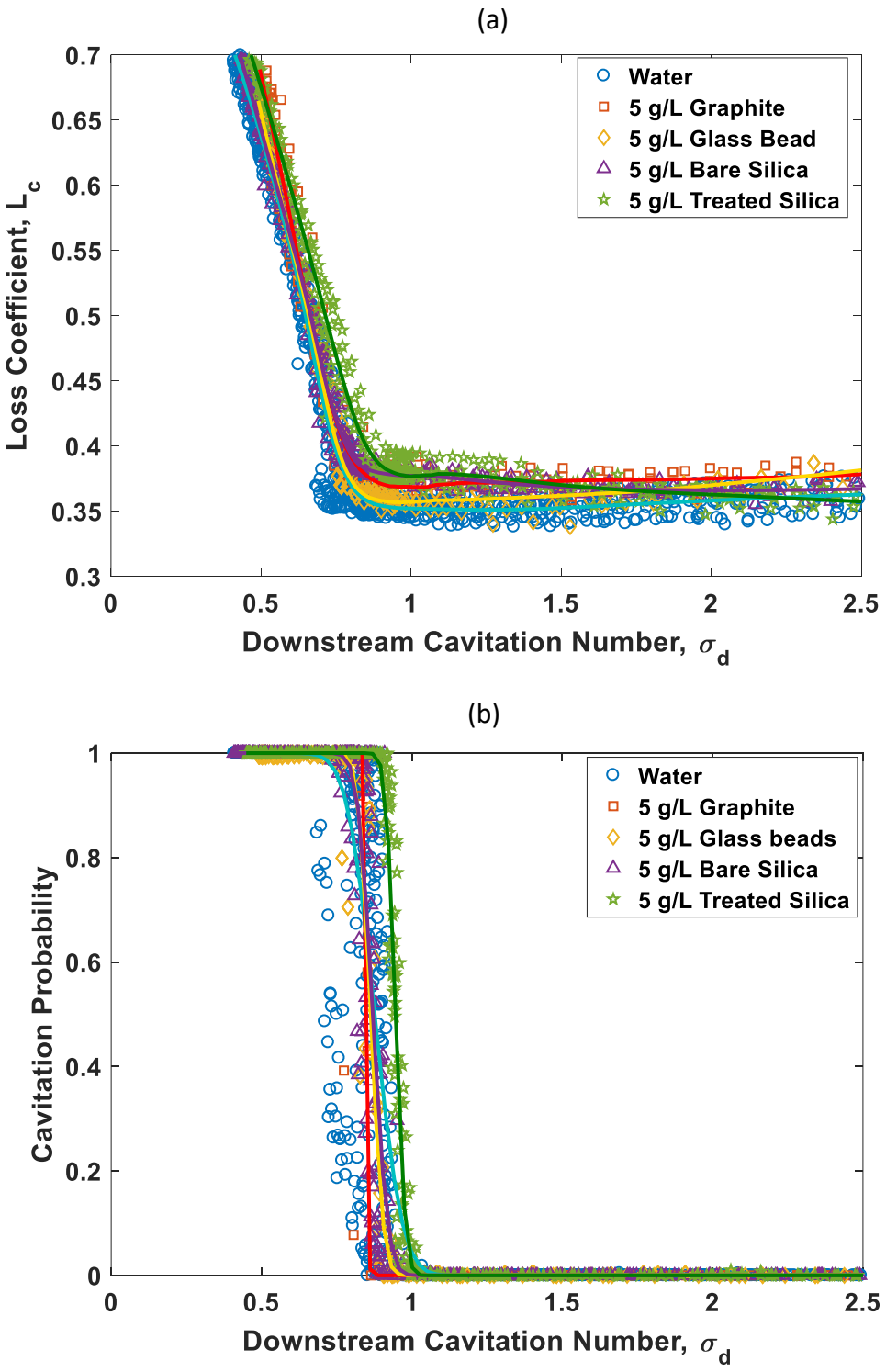

Figure 5-8. (a) Loss coefficient and (b) cavitation scale in terms of downstream cavitation number with particles at 5 g/L.

5.5. Effects of gas injection on cavitation behaviors

As discussed in section 2.4, a bubble or cavity with a radius smaller than the critical value would significantly reduce the required pressure drop for bubble growth. If the bubble has a radius higher than the critical value with certain tensile strength applied, the growth would become spontaneous as the nucleation energy barrier has been overcomed. Either way, the pre-existing bubbles can enhance cavitation activities. To experimentally demonstrate this theory, nitrogen gas was injected from 5 cm upstream of the Venturi tube at constant flow rates. The injected gas enters the system through passing a porous mesh where it gets scattered into small bubbles.

The cavitation inception measurement by using acoustic method is shown in Figure 5-9. The injection of bubbles significantly enhanced cavitation inception as the cavitation probability curves are shifted to lower velocities. As the gas injection rate increased from 0.2 LPM to 0.5 LP, the inception velocity is further decreased. Comparing to the base run of water where the cavitation probability curve shows a steep rise in the narrow range from 15 m/s to 16m/s, the injection of gas stretched the range from 4 m/s to 14 m/s. Acoustic energy received at low velocity could be due to the collapse of injected bubbles. As it is difficult to identify the inception value based the wide range of cavitation probability, the examination of the loss coefficient curves are required.

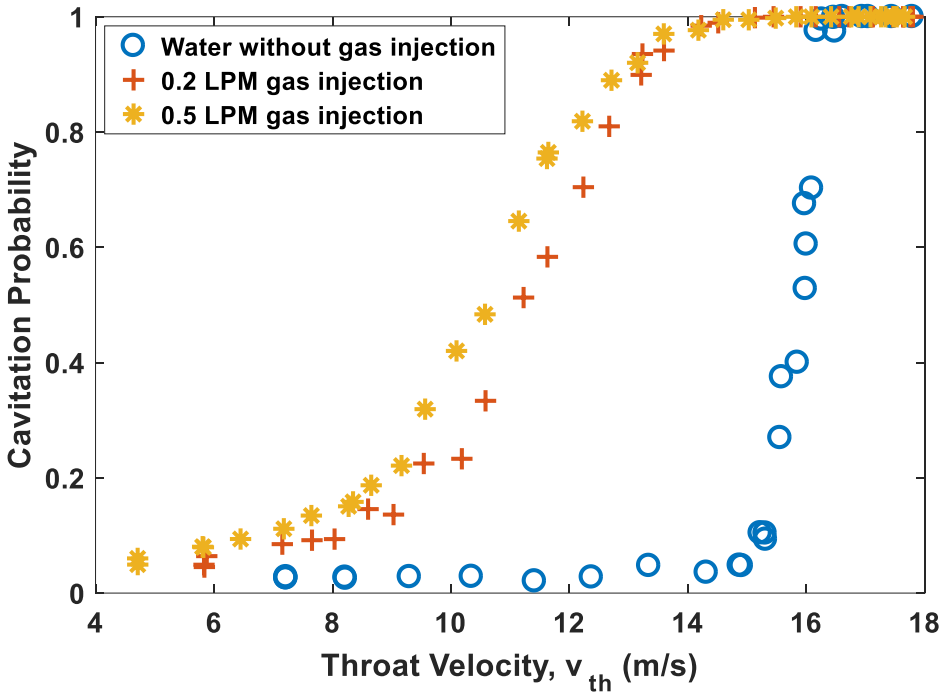

Figure 5-9. Cavitation probability vs. throat velocity with and without bubble injection.

The loss coefficient against cavitation number of water with and without bubble injection are plotted in Figure 5-10. The effect of gas injection on the flow rate and density of the fluid mixture were taken into account in the calculation of dimensionless numbers. As shown in Figure 5-10, the presence of pre-existing bubbles has two effects on the Lc curve. First, the system resistance become higher with the increase in gas flow rate, which could be due to the blockage effect caused by the bubbles. Second, the inception number of water increased from 0.75 to about 1 with 0.2 LPM of gas injection, and 1.3 with 0.5 LPM of gas injection. In terms of throat velocity, the cavitation inception of water was decreased from about 15.5 m/s to 13.5 m/s and 13 m/s with the two rates of gas injection. As proved by the experimental results, the

presence of bubbles can significantly reduce the tensile strength required to overcome the energy barrier, thereby promoting cavitation at relatively high pressure and low throat velocity.

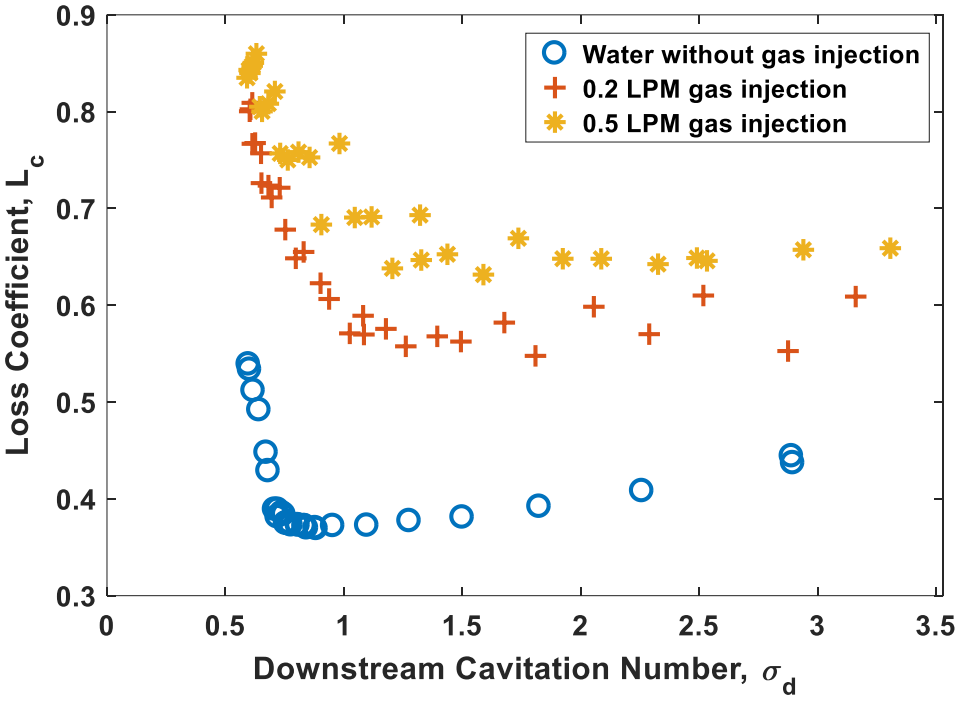

Figure 5-10. Loss coefficient in terms of downstream cavitation number with gas injection at different rates

Chapter 6 Conclusion and Contribution to Original Knowledge

6.1 Conclusion

A geometric optimization of Venturi tubes regarding hydrodynamic cavitation was performed using both simulations and experiments. The divergent angle and the diameter ratio were found to be the two key parameters to decrease the throat pressure and the power consumption. Using dimensionless numbers, two hydrodynamic regimes were identified in experiments: a single-phase geometry-dependent regime at low throat velocity and a cavitating flow at high throat velocity independent of the geometry. In the first regime, the flow resistance (dimensionless pressure difference) is constant and increases with the divergent angle while in the cavitating regime all loss coefficients increase and collapse into a single curve. The cavitation inception corresponds to the intersection between these two regimes and is set by the loss coefficient before cavitation. Higher flow resistance results in higher inception velocity.

Under cavitating flow, the bubble generation scales linearly with the extra loss induced by cavitation (difference between the loss coefficient in the cavitating regime and the single-phase flow) and with the dissolved gas concentration. This confirms the universal behavior under cavitation for all the tested geometries. The efficiency of a Venturi tube to transfer the flow energy to the cavitation is characterized by the cavitation loss and depends on the single-phase flow resistance. Thus, the cavitation inception and activity (bubble generation and collapse) are governed by the Venturi tube geometry through the loss coefficient before cavitation. Consequently, a powerful way to design efficient cavitation Venturi tubes is to decrease the single-phase flow resistance by lowering the divergent angle.

The particles' effect on hydrodynamic cavitation behavior was reflected by the change in loss coefficient and cavitation probability. By adding particles into cavitation system, the scattered inception values become consistent due to the increase in nucleation sites. The change in particle concentration did not show any obvious impact on the hydrodynamic behaviors except for the flow resistance. The hydrophobic treatment of particle, on the other hand, lowered the cavitation inception. Different types of particles were also tested under cavitation and confirmed the wettability to be the most significant particle property in affecting cavitation behavior. The pre-existing bubble's effect on cavitation behavior was demonstrated in the bubble injection experiment and earlier inceptions were observed with the increase in injection rate.

6.2 Contribution to original knowledge

In the previous Venturi tube geometry study, most investigations were performed by using CFD simulation. In this study, 3D printing technology allows us to fabricate tubes quickly with different geometries, so the Venturi tube geometry's effect on hydrodynamic cavitation could be experimentally tested. The innovative methods of acoustic detection and high-speed photography were used to measure the cavitation inception and bubble generation rate respectively. The experimental results confirmed the trend described in simulation study, and the dimensionless numbers such as loss coefficient and cavitation number were used so that the behavior of hydrodynamic cavitation with different tube geometries could be globally described.

For the study of particle-cavitation interaction, most of the previous researches were conducted by applying acoustic cavitation on substances in a static liquid condition. In this study, particles with different properties were added to the flow under hydrodynamic cavitation. The change in cavitation behaviors was described by using the dimensionless numbers and cavitation probability. The results in this study provided better understanding of the synergy between particle properties and hydrodynamic cavitation behaviors.

Chapter 7 Future Work

1) In the geometry study, lowering the Venturi tube outlet angle can reduce flow turbulence at the throat outlet, thereby enhancing cavitation through decreasing the inception and increasing the bubble generation rate. In the flotation industry, bubbles are generated for collecting particles, and turbulence at the tube outlet might provide strong force field to help bubble/particle attachment. Therefore, it would be an interesting topic to find the optimization of outlet angle so that it is as low as possible to enhance bubble generation, meanwhile large enough to provide turbulence for bubble/particle interaction.
2) In the preliminary single-phase simulation study, Venturi tube inlet angle and throat length have a negligible impact on pressure change inside the tube. However, turbulence inside the throat might be induced if the inlet angle is large enough. Also, by increasing the throat length, the fluid would spend longer period under low-pressure condition, which is beneficial for bubble growth. Therefore, it is also necessary to experimentally test the effects of tube inlet angle and throat length on cavitation behavior and size of generated bubbles.
3) Besides of the Venturi tube geometry, the roughness of the inner tube wall would also be an interesting parameter to look at. Since the rough surface would increase the tube resistance, at the same time provides crevices to enhance bubble generation, it affects cavitation from both positive and negative sides. Tests would be required to investigate which effect would be more dominant.

4) The Venturi tube geometry study was performed with lab-scale tubes. To apply the results in industry-scale applications, a scale-up test must be done to ensure the consistency of cavitation behaviors with difference sizes of tubes.
5) In the particle addition study, due to the limitation of flow meter, cavitation tests were performed with particles at relatively low concentration compared to the mineral processing industry. The change in fluid density and viscosity would become influential to hydrodynamic cavitation behaviors with further increase in the particle concentration. To have a better understanding of this effect, particles with higher concentration need to be tested in the future search.
6) The particle addition effect on hydrodynamic cavitation was monitored through the change in inception and dimensionless numbers. However, the fundamental study of bubble/particle interaction behaviors was not performed. If applicable, real-time dynamics of bubble formation needs to be monitored by using a high-speed camera shooting through a transparent Venturi tube. This study would give us better understanding of bubble/particle interaction and location of bubble formation.
7) The implementation of hydrodynamic cavitation in fine particle flotation was proved beneficial in previous researches. However, the fundamental cause for the recovery increase still has not been clearly indicated. In cavitation process, the micron bubbles improve bubble/particle attachment through two theoretical processes: forming agglomerations of fine particles to increase the collision probability, or bridging the fine particle and flotation bubbles to increase the attachment probability. To demonstrate these causes, experiments need to be designed and tested in the future.

References

S. Arrojo and Y. Benito, “A theoretical study of hydrodynamic cavitation,” *Ultrason. Sonochem.*, vol. 15, no. 3, pp. 203–211, 2008.

A. P. A Mahulkar, “Analysis of hydrodynamic and acoustic cavitation reactors.” Germany: VDM publishing, 2010.

A. Agarwal, W. J. Ng, and Y. Liu, “Principle and applications of microbubble and nanobubble technology for water treatment,” *Chemosphere*, vol. 84, no. 9, pp. 1175–1180, 2011.

R. Ahmadi, D. A. Khodadadi, M. Abdollahy, and M. Fan, “Nano-microbubble flotation of fine and ultrafine chalcopyrite particles,” *Int. J. Min. Sci. Technol.*, vol. 24, no. 4, pp. 559–566, 2014.

G. V. Ambulgekar, S. D. Samant, and A. B. Pandit, “Oxidation of alkylarenes using aqueous potassium permanganate under cavitation: Comparison of acoustic and hydrodynamic techniques,” *Ultrason. Sonochem.*, vol. 12, no. 1–2 SPEC. ISS., pp. 85–90, 2005.

A. Andersen and K. A. Mørch, “Cavitation nuclei in water exposed to transient pressures,” *J. Fluid Mech.*, vol. 771, pp. 424–448, 2015.

A. Andersen *et al.*, “Role of hydrodynamic cavitation in fine particle flotation,” *Int. J. Miner. Process.*, vol. 22, no. 4, pp. 139–149, 2015.

C. Anh Ho and M. Sommerfeld, “Modelling of micro-particle agglomeration in turbulent flows,” *Chem. Eng. Sci.*, vol. 57, no. 15, pp. 3073–3084, 2002.

K. B. Ansari *et al.*, “Process Intensification of Upgradation of Crude Oil and Vacuum Residue

by Hydrodynamic Cavitation and Microwave Irradiation," *Indian Chem. Eng.*, vol. 57, no. 3–4, pp. 256–281, 2015.

R. E. Apfel, "The Role of Impurities in Cavitation-Threshold Determination," *J. Acoust. Soc. Am.*, vol. 48, no. 5B, p. 1179, 1970.

S. Arrojo, Y. Benito, and A. Martínez Tarifa, "A parametrical study of disinfection with hydrodynamic cavitation," *Ultrason. Sonochem.*, vol. 15, no. 5, pp. 903–908, 2008.

M. Ashokkumar, R. Rink, and S. Shestakov, "Hydrodynamic cavitation – an alternative to ultrasonic food processing," 2011.

S. M. Ashrafizadeh and H. Ghassemi, "Experimental and numerical investigation on the performance of small-sized cavitating Venturis," *Flow Meas. Instrum.*, vol. 42, pp. 6–15, 2015.

A. a. Atchley and A. Prosperetti, "The crevice model of bubble nucleation," *J. Acoust. Soc. Am.*, vol. 86, no. 3, p. 1065, 1989.

T. A. Bashir, A. G. Soni, A. V. Mahulkar, and A. B. Pandit, "The CFD driven optimisation of a modified Venturi for cavitational activity," *Can. J. Chem. Eng.*, vol. 89, no. 6, pp. 1366–1375, 2011.

D. Bhaga and M. E. Weber, "Bubbles in viscous liquids: shapes, wakes and velocities," *J. Fluid Mech.*, vol. 105, pp. 61–85, 1981.

R. K. Bhaskaracharya, S. Kentish, and M. Ashokkumar, "Selected applications of ultrasonics in food processing," *Food Eng. Rev.*, vol. 1, no. 1, pp. 31–49, 2009.

Biolin Scientific, “Static and dynamic contact angles and their measurement techniques,” pp. 1–3.

E. Bormashenko, R. Pogreb, G. Whyman, Y. Bormashenko, and M. Erlich, “Vibration-induced Cassie-Wenzel wetting transition on rough surfaces,” *Appl. Phys. Lett.*, vol. 90, no. 20, pp. 1–3, 2007.

S. Bose, S. Vahabzadeh, and A. Bandyopadhyay, “Bone tissue engineering using 3D printing,” *Mater. Today*, vol. 16, no. 12, pp. 496–504, 2013.

N. Bremond, M. Arora, S. M. Dammer, and D. Lohse, “Interaction of cavitation bubbles on a wall,” *Phys. Fluids*, vol. 18, no. 12, 2006.

N. Bremond, M. Arora, C. D. Ohl, and D. Lohse, “Controlled multibubble surface cavitation,” *Phys. Rev. Lett.*, vol. 96, no. 22, pp. 1–4, 2006.

S. Brinkhorst, E. von Levante, and G. Wendt, “Numerical Investigation of Effects of Geometry on Cavitation in Herschel Venturi-Tubes applied to Liquid Flow Metering,” no. April 2015, 2016.

S. Calgaroto, A. Azevedo, and J. Rubio, “Flotation of quartz particles assisted by nanobubbles,” *Int. J. Miner. Process.*, vol. 137, pp. 64–70, 2015.

J. Carpenter, M. Badve, S. Rajoriya, S. George, V. K. Saharan, and A. B. Pandit, “Hydrodynamic cavitation: an emerging technology for the intensification of various chemical and physical processes in a chemical process industry,” *Rev. Chem. Eng.*, vol. 0, no. 0, 2016.

F. Caupin and E. Herbert, “Cavitation in water: a review,” *Comptes Rendus Phys.*, vol. 7, no. 9–10, pp. 1000–1017, 2006.

E. Brennen, *Cavitation and bubble dynamics*. 2013.

E. Brennen, *Cavitation and bubble dynamics*, vol. 9, no. 1. 1995.

C. Crake *et al.*, “Enhancement and Passive Acoustic Mapping of Cavitation from Fluorescently Tagged Magnetic Resonance-Visible Magnetic Microbubbles In??Vivo,” *Ultrasound Med. Biol.*, vol. 42, no. 12, pp. 3022–3036, 2016.

J. J. Da Rosa and J. Rubio, “The FF (flocculation-flotation) process,” *Miner. Eng.*, vol. 18, no. 7, pp. 701–707, 2005.

I. Demers, “Enhancing Fine Particle Recovery in Flotation,” p. 51, 2005.

J. Diao and D. W. Fuerstenau, “Characterization of the wettability of solid particles by film flotation 2. Theoretical analysis,” *Colloids and Surfaces*, vol. 60, no. C, pp. 145–160, 1991.

S. Eiamsa-ard, K. Wongcharee, and S. Sripattanapipat, “3-D Numerical simulation of swirling flow and convective heat transfer in a circular tube induced by means of loose-fit twisted tapes,” *Int. Commun. Heat Mass Transf.*, vol. 36, no. 9, pp. 947–955, 2009.

D. Feng and C. Aldrich, “Effect of particle size on flotation performance of complex sulphide ores,” *Miner. Eng.*, vol. 12, no. 7, pp. 721–731, 1999.

E. Forbes, “Shear, selective and temperature responsive flocculation: A comparison of fine particle flotation techniques,” *Int. J. Miner. Process.*, vol. 99, no. 1–4, pp. 1–10, 2011.

E. Forbes, D. J. Bradshaw, and G. V. Franks, “Temperature sensitive polymers as efficient and selective flotation collectors,” *Miner. Eng.*, vol. 24, no. 8, pp. 772–777, 2011.

D. W. Fuerstenau and M. C. Williams, “Characterization of the lyophobicity of particles by film flotation,” *Colloids and Surfaces*, vol. 22, no. 1, pp. 87–91, 1987.

D. Fuerstenau, “Characte , rization of the wettability film flotation 1 . Experimental investigation,” vol. 60, pp. 127–144, 1991.

M. Goel, H. Hongqiang, A. S. Mujumdar, and M. B. Ray, “Sonochemical decomposition of volatile and non-volatile organic compounds - A comparative study,” *Water Res.*, vol. 38, no. 19, pp. 4247–4261, 2004.

P. R. Gogate, “Hydrodynamic Cavitation for Food and Water Processing,” *Food Bioprocess Technol.*, vol. 4, no. 6, pp. 996–1011, 2011.

P. R. Gogate and A. M. Kabadi, “A review of applications of cavitation in biochemical engineering/biotechnology,” *Biochem. Eng. J.*, vol. 44, no. 1, pp. 60–72, 2009.

P. R. Gogate and A. B. Pandit, “Engineering design methods for cavitation reactors II: Hydrodynamic cavitation,” *AIChE J.*, vol. 46, no. 8, pp. 1641–1649, 2000.

P. R. Gogate and A. B. Pandit, “A review and assessment of hydrodynamic cavitation as a technology for the future,” *Ultrason. Sonochem.*, vol. 12, no. 1–2, pp. 21–27, 2005.

J. Gregory and S. Barany, “Adsorption and flocculation by polymers and polymer mixtures,” *Adv. Colloid Interface Sci.*, vol. 169, no. 1, pp. 1–12, 2011.

D. Hart and D. Whale, “A review of cavitation-erosion resistant weld surfacing alloys for

hydroturbines," *Eutectic Aust. Pty. Ltd., Sydney*, p. 15, 2007.

E. Herbert, S. Balibar, and F. Caupin, "Cavitation pressure in water," *Phys. Rev. E - Stat. Nonlinear, Soft Matter Phys.*, vol. 74, no. 4, pp. 1–22, 2006.

S. Jones, "Bubble nucleation from gas cavities — a review," *Adv. Colloid Interface Sci.*, vol. 80, no. 1, pp. 27–50, 1999.

E. Joyce, S. S. Phull, J. P. Lorimer, and T. J. Mason, "The development and evaluation of ultrasound for the treatment of bacterial suspensions. A study of frequency, power and sonication time on cultured Bacillus species," *Ultrason. Sonochem.*, vol. 10, no. 6, pp. 315–318, 2003.

K. K. Jyoti and A. B. Pandit, "Water disinfection by acoustic and hydrodynamic cavitation," *Biochem. Eng. J.*, vol. 7, no. 3, pp. 201–212, 2001.

A. Karimi and F. Avellan, "Comparison of erosion mechanisms in different types of cavitation," *Wear*, vol. 113, no. 3, pp. 305–322, 1986.

M. A. Kelkar, P. R. Gogate, and A. B. Pandit, "Intensification of esterification of acids for synthesis of biodiesel using acoustic and hydrodynamic cavitation," *Ultrason.*

R. T. Knapp, "Recent Investigations of the Mechanics of Cavitation and Cavitation Damage," *Trans. ASME*, vol. 77, pp. 1045–1054, 1955.

D. Krefting, R. Mettin, and W. Lauterborn, "High-speed observation of acoustic cavitation erosion in multibubble systems," *Ultrason. Sonochem.*, vol. 11, pp. 119–123, 2004.

P. S. Kumar and A. B. Pandit, "Modeling Hydrodynamic Cavitation," *Chem. Eng. Technol.*, vol.

22, no. 12, pp. 1017–1027, 1999.

J. M. Lee, M. Zhang, and W. Y. Yeong, “Characterization and evaluation of 3D printed microfluidic chip for cell processing,” *Microfluid. Nanofluidics*, vol. 20, no. 1, pp. 1–15, 2016.

H. Li, “Role of hydrodynamic cavitation in fine particle flotation,” *Int. J. Miner. Process.*, vol. 51, no. 1–4, pp. 139–149, 2014.

H. Li, A. Afacan, Q. Liu, and Z. Xu, “Study interactions between fine particles and micron size bubbles generated by hydrodynamic cavitation,” *Miner. Eng.*, vol. 84, pp. 106–115, 2015.

Q. Liu and Z. Xu, “Self-Assembled Monolayer Coatings on Nanosized Magnetic Particles Using

Malvern, “Mastersizer 3000,” p. 182, 2013.

C. S. Martin, H. Medlarz, D. C. Wiggert, and C. Brennen, “Cavitation Inception in Spool Valves,” *J. Fluids Eng.*, vol. 103, no. 4, p. 564, 1981.

Kosjek, Aleksandra Krivograd Klemenc, Martina Oder, Martin Petkovšek, Nejc Racki, Maja Ravnikar, Andrej Šarc, Brane Širok, Mojca Zupanc, Miha Zitnik, “Ultrasonics Sonochemistry Use of hydrodynamic cavitation in (waste) water treatment,” *Ultrason. Sonochem.*, vol. 29, pp. 577–588, 2016.

K. A. Matis, G. P. Gallios, and K. A. Kydros, “Separation of fines by flotation techniques,” *Sep. Technol.*, vol. 3, no. 2, pp. 76–90, 1993.

and K. K. Mawson, R., “A brief history of the application of ultrasonics in food processing,”

19-th ICA Congr. Madrid., 2007.

T. Miettinen, J. Ralston, and D. Fornasiero, "The limits of fine particle flotation," *Miner. Eng.*, vol. 23, no. 5, pp. 420–437, 2010.

P. J. Milly, R. T. Toledo, M. A. Harrison, and D. Armstead, "Inactivation of food spoilage microorganisms by hydrodynamic cavitation to achieve pasteurization and sterilization of fluid foods," *J. Food Sci.*, vol. 72, no. 9, pp. 414–422, 2007.

C. Mishra and Y. Peles, "An experimental investigation of hydrodynamic cavitation in micro-Venturis," *Phys. Fluids*, vol. 18, no. 10, p. 103603, 2006.

V. S. Moholkar and A. B. Pandit, "Modeling of hydrodynamic cavitation reactors: A unified approach," *Chem. Eng. Sci.*, vol. 56, no. 21–22, pp. 6295–6302, 2001.

V. S. Moholkar and A. B. Pandit, "Numerical investigations in the behaviour of one-dimensional bubbly flow in hydrodynamic cavitation," *Chem. Eng. Sci.*, vol. 56, no. 4, pp. 1411–1418, 2001.

V. S. Moholkar and A. B. Pandit, "Bubble behavior in hydrodynamic cavitation: Effect of turbulence," *AIChE J.*, vol. 43, no. 6, pp. 1641–1648, 1997.

N. P. Murphy and R. H. Petrmichl, "Hyghly durable hydrophobic coatings and methods," *Us006743516B2*, vol. 2, no. 12, 2004.

C. F. Naudé and A. T. Ellis, "On the Mechanism of Cavitation Damage by Nonhemispherical Cavities Collapsing in Contact With a Solid Boundary," *J. Basic Eng.*, vol. 83, no. 4, p. 648, 1961.

S. Paliwal and S. Mitragotri, “Ultrasound-induced cavitation: applications in drug and gene delivery,” *Expert Opin. Drug Deliv.*, vol. 3, no. 6, pp. 713–726, 2006.

L. Parkinson and J. Ralston, “Dynamic aspects of small bubble and hydrophilic solid encounters,” *Adv. Colloid Interface Sci.*, vol. 168, no. 1–2, pp. 198–209, 2011.

D. W. Peddie, “University of alberta - unofficial record,” vol. 1, pp. 1–3, 2011.

S. Perumal, Kumar, Sim Mei, “CFD Study of the Effect of Venturi Convergent and Divergent Angles on Low Pressure Wet Gas Metering,” *J. Appl. Sci.*, 2014.

D. V. Pinjari and A. B. Pandit, “Room temperature synthesis of crystalline CeO2 nanopowder: Advantage of sonochemical method over conventional method,” *Ultrason. Sonochem.*, vol. 18, no. 5, pp. 1118–1123, 2011.

J. Ralston, “Inertial hydrodynamic particle – bubble interaction in flotation,” pp. 207–256, 1999.

L. N. Randall, “Rocket Applications of the Cavitating Venturi,” *J. Am. Rocket Soc.*, vol. 22, pp. 28–38, 1952.

P. Rudolf, M. Hudec, M. Gríger, and D. Štefan, “Characterization of the cavitating flow in converging-diverging nozzle based on experimental investigations,” *EPJ Web Conf.*, vol. 2101, 2014.

M. Sadatomi, A. Kawahara, K. Kano, and A. Ohtomo, “Performance of a new micro-bubble generator with a spherical body in a flowing water tube,” *Exp. Therm. Fluid Sci.*, vol. 29, no. 5, pp. 615–623, 2005.

V. K. Saharan, M. A. Rizwani, A. A. Malani, and A. B. Pandit, “Effect of geometry of hydrodynamically cavitating device on degradation of orange-G,” *Ultrason. Sonochem.*, vol. 20, no. 1, pp. 345–353, 2013.

P. J. Sanchez-Soto *et al.*, “Talc from Puebla de Lillo, Spain. II. Effect of dry grinding on particle size and shape,” *Appl. Clay Sci.*, vol. 12, no. 4, pp. 297–312, 1997.

R. Sander, “Compilation of Henry’s law constants (version 4.0) for water as solvent,” *Atmos. Chem. Phys.*, vol. 15, no. 8, pp. 4399–4981, 2015.

A. Y. Seiji Shimizu, “EROSION IN HYDRAULIC OIL , HWCFs , AND TAP WATER,” 1989.

P. Senthil Kumar, M. Siva Kumar, and A. B. Pandit, “Experimental quantification of chemical effects of hydrodynamic cavitation,” *Chem. Eng. Sci.*, vol. 55, pp. 1633–1639, 2000.

R. Singh, S. K. Tiwari, and S. K. Mishra, “Cavitation erosion in hydraulic turbine components and mitigation by coatings: Current status and future needs,” *J. Mater. Eng. Perform.*, vol. 21, no. 7, pp. 1539–1551, 2012.

M. Sivakumar and A. B. Pandit, “Wastewater treatment: A novel energy efficient hydrodynamic cavitational technique,” *Ultrason. Sonochem.*, vol. 9, no. 3, pp. 123–131, 2002.

J. G. Slowik *et al.*, “Particle Morphology and Density Characterization by Combined Mobility and Aerodynamic Diameter Measurements. Part 2: Application to Combustion-Generated Soot Aerosols as a Function of Fuel Equivalence Ratio,” *Aerosol Sci. Technol.*, vol. 38, no. 12, pp. 1206–1222, 2004.

A. Sobhy and D. Tao, “Nanobubble column flotation of fine coal particles and associated fundamentals,” *Int. J. Miner. Process.*, vol. 124, pp. 109–116, 2013.

a Sobhy, R. Honaker, and D. Tao, “Nanobubble Column Flotation for More Efficient Coal Recovery,” vol. 507, pp. 1–7, 2013.

T. V. Subrahmanyam and K. S. E. Forssberg, “Fine particles processing: shear-flocculation and carrier flotation - a review,” *Int. J. Miner. Process.*, vol. 30, no. 3–4, pp. 265–286, 1990.

M. C. Sukop and D. Or, “Lattice Boltzmann method for homogeneous and heterogeneous cavitation,” *Phys. Rev. E - Stat. Nonlinear, Soft Matter Phys.*, vol. 71, no. 4, pp. 1–5, 2005.

K. S. Suslick, “The Chemical Effects of Ultrasound,” *Sci. Am.*, vol. 260, no. 2, pp. 80–86, 1989.

M. A. Sutton, N. Li, D. C. Joy, A. P. Reynolds, and X. Li, “Scanning electron microscopy for quantitative small and large deformation measurements Part I: SEM imaging at magnifications from 200 to 10,000,” *Exp. Mech.*, vol. 47, no. 6, pp. 775–787, 2007.

D. Tao, “Role of Bubble Size in Flotation of Coarse and Fine Particles—A Review,” *Sep. Sci. Technol.*, vol. 39, no. 4, pp. 741–760, 2005.

D. Tao, S. Yu, X. Zhou, R. Q. Honaker, and B. K. Parekh, “Picobubble Column Flotation of Fine Coal,” *Int. J. Coal Prep. Util.*, vol. 28, no. 1, pp. 1–14, 2008.

W. J. Trahar and L. J. Warren, “The flotability of very fine particles - A review,” *Int. J. Miner. Process.*, vol. 3, no. 2, pp. 103–131, 1976.

J. R. Tumbleston *et al.*, “Continuous liquid interface production of 3D objects,” *Science*

(80-.)., vol. 347, no. 6228, pp. 1349–1352, 2015.

K. D. Vernon-Parry, “Scanning electron microscopy: an introduction,” *III-Vs Rev.*, vol. 13, no. 4, pp. 40–44, 2000.

Z. W. A, “Relation of the Equilibrium Contact Angle to Liquid and Solid Constitution,” *Adv. Chem.*, vol. 43, no. 2, pp. 1–51, 1964.

L. J. Warren, “Shear-flocculation of ultrafine scheelite in sodium oleate solutions,” *J. Colloid Interface Sci.*, vol. 50, no. 2, pp. 307–318, 1975.

M. E. Weber and D. Paddock, “Interceptional and gravitational collision efficiencies for single collectors at intermediate Reynolds numbers,” *J. Colloid Interface Sci.*, vol. 94, no. 2, pp. 328–335, 1983.

Y. Xing, X. Gui, Y. Cao, D. Wang, and H. Zhang, “Clean low-rank-coal purification technique combining cyclonic-static microbubble flotation column with collector emulsification,” *J. Clean. Prod.*, vol. 3, 2016.

Y. Yan and R. B. Thorpe, “Flow regime transitions due to cavitation in the flow through an orifice,” *Int. J. Multiph. Flow*, vol. 16, no. 6, pp. 1023–1045, 1990.

X. Ye, X. Yao, and R. Han, “Dynamics of cavitation bubbles in acoustic field near the rigid wall,” *Ocean Eng.*, vol. 109, pp. 507–516, 2015.

J. Yin, J. Li, H. Li, W. Liu, and D. Wang, “Experimental study on the bubble generation characteristics for an Venturi type bubble generator,” *Int. J. Heat Mass Transf.*, vol. 91, no. November, pp. 218–224, 2015.

R. H. Yoon and G. H. Luttrell, “The Effect of Bubble Size on Fine Coal Flotation,” *Coal Prep.*, vol. 2, no. 3, pp. 179–192, 1986.

R.-H. Yoon, D. H. Flinn, and Y. I. Rabinovich, “Hydrophobic interactions between dissimilar surfaces,” *J. Colloid Interface Sci.*, vol. 185, no. 2, pp. 363–370, 1997.

X. Yu and P. Felicia, “Optimization of cavitation Venturi tube design for pico and nano bubbles generation,” *Int. J. Min. Sci. Technol.*, vol. 25, pp. 523–529, 2015.

Yusuf G. Adewuyi, “Sonochemistry: Environmental Science and Engineering Applications,” *Ind. Eng. Chem. Res*, no. 40, pp. 4681–4715, 2001.

W. Zhou, H. Chen, L. Ou, and Q. Shi, “International Journal of Mineral Processing Aggregation of ultra- fi ne scheelite particles induced by hydrodynamic cavitation,” *Int. J. Miner. Process.*, vol. 157, pp. 236–240, 2016.

Z. A. Zhou, Z. Xu, and J. A. Finch, “On the role of cavitation in particle collection in flotation - A critical review,” *Miner. Eng.*, vol. 22, no. 5, pp. 419–433, 1994.

Z. a. Zhou, Z. Xu, J. a. Finch, H. Hu, and S. R. Rao, “Role of hydrodynamic cavitation in fine particle flotation,” *Int. J. Miner. Process.*, vol. 51, no. 1–4, pp. 139–149, 1997.

Z. A. Zhou, Z. Xu, J. A. Finch, J. H. Masliyah, and R. S. Chow, “On the role of cavitation in particle collection in flotation – A critical review. II,” *Miner. Eng.*, vol. 22, no. 5, pp. 419–433, 2009.